Morphology and structure of spherically propagating premixed turbulent hydrogen – air flames

Shehab, Hazim
Department of Advanced Environmental Science and Engineering, Kyushu University

Watanabe, Hiroaki
Department of Advanced Environmental Science and Engineering, Kyushu University

Minamoto, Yuki
Department of Mechanical Engineering, Tokyo Institute of Technology

Kurose, Ryoichi
Department of Mechanical Engineering and Science, Kyoto University

他

https://hdl.handle.net/2324/7162483

出版情報：Combustion and Flame. 238, pp.111888-, 2022-04. Elsevier
バージョン：
権利関係：

Morphology and Structure of Spherically Propagating Premixed Turbulent Hydrogen – Air Flames

Hazim Shehab*[a], Hiroaki Watanabe[b,c], Yuki Minamoto[d], Ryoichi Kurose[e] and Toshiaki Kitagawa[a]

[a]Department of Mechanical Engineering, Graduate School of Engineering, Kyushu University, 774 Motooka, Nishi-ku, Fukuoka 819-0395, Japan

[b]Department of Advanced Environmental Science and Engineering, Kyushu University, 6-1 Kasuga-koen, Kasuga, Fukuoka 816-8580, Japan

[c]International Institute for Carbon-Neutral Energy Research, Kyushu University, 774 Motooka, Nishi-ku, Fukuoka 819-0395, Japan

[d]Department of Mechanical Engineering, Tokyo Institute of Technology, 2-12-1 Ookayama, Meguro, Tokyo 152-8550, Japan

[e]Department of Mechanical Engineering and Science, Kyoto University, Kyoto daigaku-Katsura, Nishikyo-ku, Kyoto 615-8540, Japan

---

*Corresponding author
Present address: Research Institute of Advanced Industrial Science and Technology (AIST), 1-2-1 Namiki, Tsukuba, Ibaraki 305-8564, Japan
Email address: hazim.shehab@aist.go.jp (Hazim Shehab)

Abstract

Three-dimensional direct numerical simulations of spherically propagating premixed turbulent stoichiometric hydrogen-air flames with detailed chemistry and detailed diffusion are employed to clarify the influence of turbulence-flame interactions with respect to flame structure and morphology. Four cases are considered within the corrugated flamelets and the thin reaction zone regimes. The most significant fuel consumption and heat release rates occur at the negatively-curved flamelets. Furthermore, the increments in burning velocity are lower than the increments in flame surface area, which is due to the reduction in the local burning intensity at the positively-curved flamelets. The morphology of intense reaction zones is quantified using Minkowski functionals and their shapes include "tubes", "pancakes" and more complex shapes, which are compared to their counterparts in planar flames. As turbulence level increases, the number of locally defined intense reaction zones increases, and their boundaries expand to cover more extensive parts of the flame front. However, intense reaction zones' geometrical dimensions do not significantly differ for each flame as it propagates. Local turbulence properties are obtained for each intense reaction zone. The conditional averages of local Taylor microscale and local Kolmogorov scale, conditioned based on the shapefinders, are investigated. The conditional averages of the local Taylor microscale scale correlate with the planarity and filamentarity of intense reaction zones. Therefore, turbulent motions at Taylor microscale size have a significant role in characterizing turbulence-flame interactions relevant to flame morphology and relevant to the local flame thickness and reaction layers of developing-flames. On the other hand, local Kolmogorov scales' turbulent motions show weaker or no such correlations. There is a dissidence between global turbulence statistics and local ones representing the interactions at the flame front. Local turbulence-flame interactions of Taylor microscale sizes occur at specific length scales, depending on the flame size and irrelevant of eddies with other length scales.

Keywords: Direct Numerical Simulation (DNS), Turbulent premixed flame, Developing flame, Spherical flame, Flame morphology, Flame structure

1 Introduction

Premixed turbulent combustion is widely used in practical applications such as power gas turbines and spark-ignition engines. Limiting harmful emissions in those applications is prioritized in order to achieve cleaner energy sources. Therefore, clarifying the implications of turbulence on flame morphology, topology, and reaction zone structure is essential to realize such priorities. Early publications related to flame morphology were discussed via fractal characteristics [1, 2, 3, 4]. The focus was mainly on predicting the flame surface properties to provide a more accurate estimation of the overall flame front area and burning velocity. Using modern and recent computational technology, numerical studies of reaction zone topology or morphology of turbulent flame fronts have become popular. Through statistical approaches, the investigation of flame-flame interactions and isolated pocket formation within turbulent flames became available through compiling a set of possible flame-flame interactions [5, 6]. Recently, Minkowski functionals and shapefinders were employed in investigating the local topology and flame morphology of MILD, premixed planar, and swirl-stabilized flames [7, 8, 9]. Experimentally, Tyagi et al. [10] have quantified the two-dimensional topology of flame-flame interactions in dual-burner flames and showed that small-scale interactions are more frequent than large-scale interactions. The previous examples show that the available literature discussed the overall morphology/topology and the morphology/topology of local flame structures of premixed turbulent flames with fully-developed flame fronts.

As for temporarily developing-flame fronts (e.g., spherical flames), the morphology/topology is usually introduced through fractal analysis and by presenting various global models for the turbulent burning speed [11, 12, 13, 14, 15, 16]. However, as the mentioned methodologies focus on the overall flame surface properties, the discussion related to the development of local flame structures would be limited. On the other hand, with DNS, it is possible to investigate local turbulence-flame interactions in developing-flame fronts, such as the local variations in burning rates and turbulent stretching effects, as well as the global evolution of the flame surface and brush thickness [17, 18, 19, 20, 21, 22, 23, 24]. However, in many studies, to reduce the huge cost of the DNS, (i) single-step chemistry or reduced reaction mechanisms were used instead of detailed chemistry, (ii) single/fixed Lewis number assumption was used instead of detailed diffusion, and/or (iii) resolution was reduced. In that regard, Aspden et al. [25] showed the importance of utilizing detailed chemistry and diffusion, as they identified a decorrelation between fuel consumption rate and heat release rate in lean hydrogen flames and related it to specific elementary reactions. Such changes to elementary reactions' response, which may not be observed in simplified chemistry, are reported to change the local species concentration, fuel consumption rate, and heat release rate within the flame. Furthermore, Aspden [26] showed that simplifying the diffusion could alter the local chemistry and consequently changing species concentrations, local fuel consumption rate, heat release rate, and the overall propagation speed of the flame. From above, it is clear that the combined utilization of detailed chemistry and diffusion is important to investigate the local properties of premixed flames, especially concerning the morphology/topology of local flame structures of developing-flame fronts which are rarely discussed.

Concerning small-scale turbulence–flame interaction in premixed flames, Gülder [27] has investigated the influences of microscale mixing within the preheat layer on local burning velocity. They concluded that the influence of turbulent eddies with Taylor microscale sizes is limited to stirring the preheat layer by contributing to transport enhancements and that it may or may not be able to wrinkle the flame front. However, Minamoto et al. [8, 9] have demonstrated that turbulent eddies scaled by Taylor microscale can contribute to flame front wrinkling, ultimately leading to an increase in turbulent burning velocity. That being said, the previously discussed works were concerned with fully-developed flames and, in the case of [7], diffusion was simplified by using the non-unity constant Lewis number assumption. As for developing-flame fronts, Kulkarni and Bisetti [28] and Kulkarni et al. [29], have investigated the surface morphology and the evolution of the brush thickness of spherical turbulent flames, and they proposed a scaling of the turbulent flame speed with the Taylor microscale Reynolds number, which can emphasises to the importance of small-scale turbulence-flame interactions in developing flame fronts. Furthermore, they showed the possibility of having a wrinkling scale that is smaller than the Taylor microscale. Still, the conducted analyses considered the global evolutions of the flame surface and brush thickness with less emphasis on the development of local flame structures. Furthermore, as the spherical flames propagated, the temporal change in turbulence scales and intensities were globally evaluated without an estimation of their values at the flame front. Thus, the extent of influence that small-scale local turbulence-flame interactions hold on developing-flame fronts needs further investigation.

The present study is focused on the local turbulence-flame interactions and the local morphology/topology of flame structures in spherically expanding premixed turbulent flames by means of DNS with the detailed chemistry and diffusion. Hydrogen-air combustion is targeted to provide comprehensive information in terms of the promotion of the clean/green energy sources. The focus is on small-scale (Taylor microscale and Kolmogorov length scale) turbulence-flame interactions concerning local flame structure and morphology. The study employs Minkowski functionals and shapefinders to quantify various shapes of the reaction zones at multiple flame sizes, which also gives the possibility of spatially evaluating turbulence statistics at the flame front. Therefore, the results give a unique insight into answering essential questions regarding (i) the evolution of the geometrical dimensions of formed local structures within the reaction layer as developing-flame fronts propagate, (ii) the dominant factors turbulent motions have on developing-flame front's morphology and structure, and (iii) the comparison between global turbulence statistics and local ones at the flame front as the developing-flame fronts propagate. In this study, "flame structure" describes microscale flame structure relevant to the local flame thickness and reaction layers, and "flame morphology" is used to describe the global flame structure, including flame shape and wrinkling.

2 Methodology

2.1 Governing equations and numerical methods

Spherically propagating hydrogen-air premixed turbulent flames were investigated employing three-dimensional direct numerical simulation with detailed chemistry and detailed diffusion. The considered flow is a weakly-compressible reactive flow where low-Mach number is assumed and can be described using the governing equations of mass, momentum, energy, and mass fraction of species as in Eqs. (1–5).

$$\frac{\partial \rho}{\partial t} + \frac{\partial \rho u_i}{\partial x_i} = 0 \tag{1}$$

$$\frac{\partial \rho u_i}{\partial t} + \frac{\partial \rho u_i u_j}{\partial x_j} = -\frac{\partial P}{\partial x_i} + \frac{\partial}{\partial x_j}\tau_{ij} \tag{2}$$

$$\begin{aligned}\frac{\partial \rho h}{\partial t} + \frac{\partial \rho u_i h}{\partial x_i} =& \frac{\partial P}{\partial t} + u_i \frac{\partial P}{\partial x_i} \\ &+ \frac{\partial}{\partial x_i}\left[\rho D_h \left(\frac{\partial h}{\partial x_i} - \sum_k \left(h_k \frac{\partial Y_k}{\partial x_i}\right)\right) - \rho \sum_k \left(h_k Y_k V_{k,i}\right)\right] + \tau_{ij}\frac{\partial u_i}{\partial x_i}\end{aligned} \tag{3}$$

$$\frac{\partial \rho Y_k}{\partial t} + \frac{\partial \rho u_i Y_k}{\partial x_i} = -\frac{\partial}{\partial x_i}\left(\rho V_{k,i} Y_k\right) + \rho \dot{\omega}_k \tag{4}$$

$$P = \rho R T \tag{5}$$

Here, ρ is the density, u_i is the velocity in i direction, P is the pressure, τ_{ij} is the viscous stress tensor, h is the specific enthalpy of the gas mixture, h_k is the specific enthalpy of species k, Y_k is the mass fraction of species k, $\dot{\omega}_k$ is the reaction rate of species k, T is the temperature and R is the universal gas constant. The thermal diffusivity, D_h is expressed as in Eq. (6).

$$D_h = \frac{\lambda_{th}}{\rho C_p} \tag{6}$$

Here, λ_{th} and C_p are the thermal conductivity and specific heat capacity at constant pressure of the mixture, respectively. The diffusion velocity of species k in i direction, $V_{k,i}$ is evaluated using the Curtiss–Hirschfelder first-order approximation [30, 31] as in Eq. (7).

$$V_{k,i} = -\frac{D_k}{X_k}\nabla X_k \tag{7}$$

where X_k is the molar fraction of species k and D_k is the molecular diffusivity of species k, and is obtained as in Eq. (8).

$$D_k = \frac{1 - Y_k}{\sum_{j \neq k} X_j / D_{jk}} \tag{8}$$

where D_{jk} is the binary diffusion coefficient of species j into species k. The term ∇X_k in Eq. (7) is evaluated using LU decomposition [32] as in Eq. (9).

$$\nabla X_k = \sum_{j \neq k} \left[\frac{X_j X_k}{D_{jk}} \left(V_j - V_k \right) \right] \tag{9}$$

The local Lewis number for each species, Le_k was obtained as shown in Eq. (10), where it compares the thermal diffusivity of the flow field, D_h to the molecular diffusivity of species k.

$$Le_k = \frac{D_h}{D_k} \tag{10}$$

The simulations were performed using an in-house thermal flow analysis code called FK^3 [33, 34, 35, 36, 37]. The FK^3 code employs a pressure-based semi-implicit solver for compressible flows, whose algorithm consists of a fractional-step method [38]. All spatial derivatives, except the convective terms in the transport equations for energy and species mass fraction, were discretized using a sixth order central difference scheme. A fifth order weighted essentially non-oscillatory (WENO) scheme was used for the convective terms in the transport equations for energy and species mass fraction to avoid any unphysical numerical oscillation [39]. For time integration, a third order Runge-Kutta scheme was used. The integration of chemical reaction rates used in the detailed chemical mechanism was preformed using an efficient stiff solver DVODE [40]. Hydrogen-air flames were implemented using an improved $H_2 - O_2$ reaction mechanism [41]. The mechanism contains 20 elementary reactions and 10 species.

2.2 Computational cases

Four cases were set up in the present study. Premixed turbulent hydrogen-air flames were investigated in stoichiometric condition, $\phi = 1.0$, with an initial temperature, T_i and pressure,

P_i of 298 K and 0.1 MPa, respectively. Homogeneous and isotropic turbulent velocity fields were generated through spectral method based on the energy spectrum function in Eq. (11) [42].

$$E_k = \frac{32}{3}\sqrt{\frac{2}{\pi}}\frac{{u'_{ini}}^2}{k_e}\left(\frac{k}{k_e}\right)^4 exp\left[-2\left(\frac{k}{k_e}\right)^2\right] \tag{11}$$

Here, ${u'}_{ini}$ is the initial turbulence intensity and k_e is the wavenumber corresponding to the initial integral length scale, $l_{E,ini}$ as, $k_e = (2\pi/l_{E,ini})$. Following that, fully developed homogeneous and isotropic turbulence fields were obtained by using the method mentioned in [43], where initial turbulence fields are developed in a freely decaying non–reactive computation. Representative turbulence properties of the fully developed turbulence fields are mentioned in Table 1. They were extracted from the three-dimensional domain of each case before starting the combustion event as averaged quantities. Here, $u' = \left(\left\langle (u_i - \langle u_i \rangle)^2 \right\rangle /3\right)^{1/2}$ is the RMS of velocity and $l_E = u'^3/\varepsilon$, $\lambda = \frac{1}{3}\sum_{i=1}^{3}\sqrt{\left\langle u_i'^2 \right\rangle / \left\langle (\partial u_i'/\partial x_i)^2 \right\rangle}$ and $\eta = \left(\nu^3/\varepsilon\right)^{1/4}$ are the integral length scale, Taylor microscale and Kolmogorov length scale, respectively. Here, ε is turbulence kinetic energy dissipation rate and ν is the kinematic viscosity. The brackets $\langle \cdot \rangle$ correspond to the space averaging operation, which is equivalent to the time averaging operation with the current homogeneity condition of the flow field [44]. In Table 1, turbulence length scales were normalized by the flame thermal thickness, δ_{th} which was obtained from the laminar flame solution (to be introduced in Section 2.3) as $\delta_{th} = (T_b - T_u)/([dT/dx]|_{max})$, and was equal to 0.35 mm. T_b is the burned gas temperature and T_u is the unburned mixture temperature. The Karlovitz number and Damköhler number are defined as $Ka = (u'/u_l)^{3/2}/(l_E/\delta_F)^{1/2}$ and $Da = (l_E/\delta_F)/(u'/u_l)$, where δ_F is Zel'dovich thickness, $\delta_F = \nu/u_l$. Re_t is the turbulent Reynolds number, $Re_t = Ka^2 Da^2$, and Re_λ is the Taylor microscale Reynolds number, $Re_\lambda = u'\lambda/\nu$. Cases C1 and C2 are classified within the corrugated flamelets regime on Peters turbulent combustion regime diagram. Case C3 is at the border between the corrugated flamelets and the thin reaction zone regimes, and case T1 is in the thin reaction zone regime, as shown in Fig. 1.

The DNS has been performed to propagate spherical turbulent premixed flames in a cubical domain with uniform mesh. All domain boundaries were set to outflow conditions. Each edge

Table 1: Numerical conditions for the present DNS cases.

Case	u'/u_l	$l_E/\delta_{F(l_E/\delta_{th})}$	$\lambda/\delta_{F(\lambda/\delta_{th})}$	$\eta/\delta_{F(\eta/\delta_{th})}$	Da	Ka	$Re_{t(Re_\lambda)}$	$k_{max}\eta$
C1	1.78	$323_{(10.3)}$	$41.9_{(1.33)}$	$2.48_{(0.08)}$	181.5	0.13	$575_{(75)}$	3.47
C2	4.71	$502_{(16.0)}$	$31.2_{(0.99)}$	$1.33_{(0.04)}$	107.0	0.45	$2366_{(147)}$	1.86
C3	6.91	$493_{(15.7)}$	$24.8_{(0.79)}$	$0.99_{(0.03)}$	71.4	0.82	$3408_{(171)}$	1.39
T1	13.66	$655_{(20.8)}$	$18.5_{(0.59)}$	$0.74_{(0.02)}$	47.9	1.97	$8945_{(252)}$	1.04

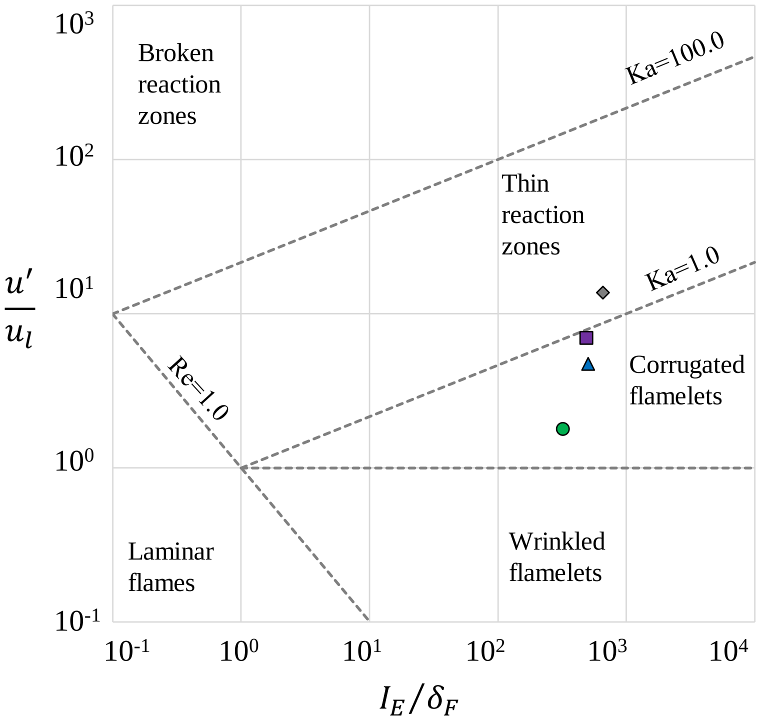

Figure 1: Regime diagram of turbulent premixed combustion [45]. Symbols denote turbulent combustion conditions for C1 (circle), C2 (triangle), C3 (square) and T1 (diamond).

was set to 16 mm in length and resolved within 640 grids, resulting in a grid resolution of 0.025 mm per grid. Those numerical settings provide 14 mesh points in all directions to resolve stoichiometric hydrogen-air laminar flame thermal thickness, δ_{th}. Additionally, those numerical settings give $k_{max}\eta$ greater than unity, as shown in Table 1, where k_{max} is the largest resolved wavenumber. Thus, assuring resolving the dissipative motion of turbulence [46].

A high-temperature region was placed at the center of the computational domain to substitute for spark energy and was only implemented at the start of computations. The region is a spherical geometry with an outer diameter of 3.0 mm and contained unburned mixture with a maximum temperature of 1500 K. The maximum temperature was set throughout the spherical geometry, from its center to a diameter of 2.0 mm, followed by a linear distribution to a diameter of 3.0 mm. Klein et al. [20] reported that varying the radius of the initial flame kernel can significantly influence the mean burning speed. Therefore, previously mentioned settings were applied to all investigated conditions. Furthermore, the current settings of the initial flame kernel were conditioned to provide the most accurate reproduction of a spherical laminar flame with the same thermochemical properties as shown in Section 2.3. The assessment of the effects of the used initial kernel on simulated flames is presented in the supplementary material.

Presented cases were performed by parallel computation on ITO computer of Kyushu University (Fujitsu PRIMERGY CX2550/CX2560 M4). For each case, the wall clock time was roughly 800 h with 1024 cores.

2.3 Laminar and turbulent flames properties

Preliminary computation was conducted to obtain the unstretched laminar burning velocity, u_l and flame thermal thickness, δ_{th}. The computation was done for the stoichiometric condition with the same initial pressure and temperatures as turbulent conditions. The computational domain used for turbulent cases was used in simulating the laminar flame, and outflow boundary conditions were applied to all domain boundaries. Laminar burning velocity, for spherically propagating flames, was obtained from the evolution of laminar flame radius, r_f as in Eq. (12).

$$u_n = \left(\frac{\rho_b}{\rho_u}\right)\left(\frac{dr_f}{dt}\right) \tag{12}$$

The burned gas density, ρ_b was obtained as the mean density of the volume enclosed by the flame front. Similarly, the unburned mixture density, ρ_u was obtained as the mean density of the volume outside the flame front. ~~Here, ρ_b and ρ_u are the burned gas density and the unburned mixture density, respectively, and were evaluated at the adiabatic flame temperature T_{ad} (for ρ_b) and T_i (for ρ_u).~~ Obtained laminar burning velocity was subjected to flame stretch due to flame front curvature and hydrodynamic strain [47, 48]. Mean flame stretch rate, α

was calculated as in Eq. (13).

$$\alpha = \left(\frac{1}{A_l}\right)\left(\frac{dA_l}{dt}\right) = \left(\frac{2}{r_f}\right)\left(\frac{dr_f}{dt}\right) \tag{13}$$

Then, the unstretched laminar burning velocity, u_l was obtained for a stretch rate of zero (=1.97 m/s). The unburned and burned Markstein numbers were obtained as $Ma \approx 0.21$ and $Ma_b \approx 0.6$, respectively. Details of their evaluation can be found in the supplementary document. Obtained values of u_l and Ma were the same as in the reported experimental results [50]. Therefore, accurately replicating the global consumption rate and flame stretch. For the current stoichiometric mixture, the effective Lewis number, $Le_{eff}(= 1.1)$ was evaluated as an average of the individual Lewis numbers of fuel (Le_{H2}) and oxidizer (Le_{O2}) obtained from Eq.(10) [51].

The turbulent burning velocity, u_t of spherically propagating premixed turbulent flame was obtained from evolution of mean turbulent flame radius, $r_{f,t}$ as shown in Eq. (14).

$$u_t = \left(\frac{\rho_b}{\rho_u}\right)\left(\frac{dr_{f,t}}{dt}\right) \tag{14}$$

Similar to experimental approach [52], mean turbulent flame radius, $r_{f,t}$ was computed from the sphere of volume equivalent to the burned gas volume. Burned gas volume was defined to be all volume within the turbulent flame front. The turbulent flame front has an area of A_t. It was defined as the three-dimensional surface area of the 1350 K isotherm, which was evaluated by summing the surface areas of all the parts of the 1350 K isotherm in the computation cells. The isotherm of 1350 K corresponded to the maximum normalized reaction rate of fuel, $\dot{\omega}^*_{H_2} = 1.0$, in the computed laminar flame solution. Here, "*" denotes an appropriate normalization using maximum, $\dot{\omega}_{H_2}|_{max}$, and minimum, $\dot{\omega}_{H_2}|_{min}$, values of the reaction rate as in Eq. (15), where $\dot{\omega}_{H_2}|_{min} = 0$. Furthermore, the 1350 K isotherm corresponded to maximum heat release rate, HRR_{max}, where HRR is computed as in Eq. (16).

$$\dot{\omega}^*_{H_2} = \frac{\dot{\omega}_{H_2} - \dot{\omega}_{H_2}|_{min}}{\dot{\omega}_{H_2}|_{max} - \dot{\omega}_{H_2}|_{min}} \tag{15}$$

$$HRR = -\sum_{k} \left(h_k^0 \dot{\omega}_k\right) \tag{16}$$

where h_k^0 is the enthalpy of formation for species k. For all computed turbulent flames, the isotherm of 1350 K corresponded to HRR_{max} as well as all regions in the flame having $\dot{\omega}_{H_2}|_{max}$ ($\dot{\omega}^*_{H_2} = 1.0$). Thus, assuring an accurate choice of representation for the flame front, as shown in Fig. 2 (also seen in Fig. 4 in Section 3.1). Since presented flames in this study are developing-flames, the range of reaction rate value, $\dot{\omega}_{H_2}$ was getting broader as flames propagated (indicating an increase in fuel consumption). Thus, the normalized reaction rate, $\dot{\omega}^*_{H_2}$ is defined to give a comparative view at each moment of flame's development. It should be noted that for turbulent flames, the profile of $\dot{\omega}^*_{H_2}$ across local flame fronts got significantly influenced by turbulence-flame interactions. Although the isotherm of 1350 K corresponded to all regions in the flame having $\dot{\omega}_{H_2}|_{max}$ and HRR_{max}, it also corresponded to regions having $0.5 > \dot{\omega}^*_{H_2} > 1.0$.

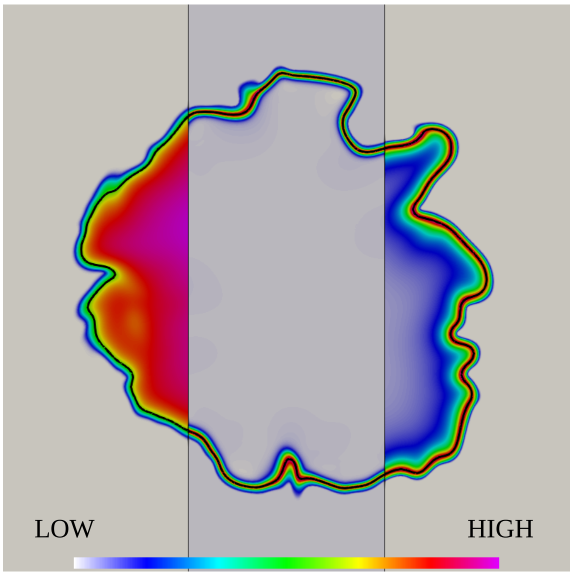

Figure 2: Central 2D slice of case C1 at $r_{f,t} = 5$ mm, showing temperature, T (left), normalized reaction rate, $\dot{\omega}^*_{H_2}$ (center) and heat release rate,HRR (right). Flame front, identified with 1350 K isotherm, is shown in "bold black line". Dimension of figure is 16 × 16 mm.

The local curvature, $\mathbb{K}$ of the spherical flames, was obtained at the flame front isosurface as $\mathbb{K} = \nabla \cdot \mathbf{n}$ [53]. Here, $\mathbb{K}$ is positive (negative) whenever the isosurface is convex (concave) in the direction of the unburned mixture as described by the local flame normal vector $\mathbf{n}$. The tangential strain rate of the flame front, a_T was obtained as $a_T = \nabla \cdot \mathbf{u} - \mathbf{nn} : \nabla \mathbf{u}$ [54].

2.4 Minkowski functionals and shapefinders

To investigate small-scale turbulence-flame interactions occurring at intense reaction zones of the flame front, shapefinders of intense reaction zones' morphology were analyzed using the Minkowski functionals [55]. Here, the shapefinders of a three-dimensional object of interest were defined with the three characteristic scales of length, $\mathcal{L}$, width, $\mathcal{W}$ and thickness, $\mathcal{T}$. The Minkowski functionals were, previously, used to analyze and identify reaction zone structures in turbulent MILD combustion, premixed swirl-stabilized flames as well as premixed planar turbulent flames [7, 8, 9]. The Minkowski functionals for each three-dimensional object are given as in Eqs. (17–20).

$$V_0 = \mathcal{V} \tag{17}$$

$$V_1 = \frac{\mathcal{S}}{6} \tag{18}$$

$$V_2 = \frac{1}{3\pi} \int_S \frac{\kappa_1 + \kappa_2}{2} \, dS \tag{19}$$

$$V_3 = \frac{1}{2\pi} \int_S (\kappa_1 \kappa_2) \, dS \tag{20}$$

Here, $\mathcal{V}$ is the volume enclosed by the surface, S, with the surface area, $\mathcal{S}$. κ_1 and κ_2 ($\kappa_1 \geq \kappa_2$) are the two principal curvatures of S. Here, V_0 and V_1 are related to the volume, $\mathcal{V}$ and surface area, $\mathcal{S}$ of the enclosed volume, while V_2 and V_3 are related to the integrated mean and Gaussian curvatures. Also, V_3 is the Euler characteristic, χ, [56] which is the topological invariant of an object. All Minkowski functionals were computed for each isolated object constructed by iso-surfaces of reaction rate by using a grid cell counting method [57]. The three characteristic scales were then obtained as in Eqs. (21). [58].

$$\mathcal{L} = \frac{3V_2}{2V_3} \quad , \quad \mathcal{W} = \frac{2V_1}{\pi V_2} \quad , \quad \mathcal{T} = \frac{V_0}{2V_1} \tag{21}$$

For a convex body, those characteristics scales have a dimension of length and are "positive semi-definite" quantities even if there is partial concavity in the structure of the object [56]. Furthermore, the three characteristics scales satisfy the inequality $\mathcal{L} \geq \mathcal{W} \geq \mathcal{T}$. Considering that Minkowski functionals have the "additivity" property [57], which leads to robustness against multiple sources of error, the same inequality applies for partially concave objects. It is also possible that an object may have an overall concave surface, leading to negative values in the principal curvatures and characteristic scales [59]. Similarly to previous investigations regarding isotropic turbulence and combustion [7, 8, 9, 56], pure concave objects were not encountered in this study. The three characteristic scales provide representative scales for an object's spatial extent and do not give the exact dimensions except for spheres [56]. As indicated in Eq. (21), the Minkowski functionals must be positive to obtain meaningful characteristic scales. However, the values of V_3 can be positive, negative, or zero because it is related to the genus, G of the object. The genus corresponds to the number of cuts that can be made along a simple curve on an object without splitting it. In a three-dimensional object, the genus corresponds to the number of holes within it and is expressed as $G = 1 - V_3/2$. For every hole in an object, value of G increases by 1. In short, $V_3 = 2$ (G=0) for an object without holes, for a torus V_3=0 (G=1) and for a pretzel $V_3 = -4$ (G=3). Hence, for objects with G>1, the characteristic scale of length, $\mathcal{L}$ represents the length between two holes in the object. For an object with non-zero genus, the characteristic scale of length, $\mathcal{L}$ should be obtained as in Eq. (22) [60].

$$\mathcal{L} = \frac{3V_2}{4\,(G+1)} \tag{22}$$

It is also possible to obtain the two dimensionless shapefinders' the planarity, $\mathcal{P}$ and the filamentarity, $\mathcal{F}$ from the three characteristic scales as in Eq. (23) [60]. For visual convenience, the geometry of a group of objects can be represented in a two-dimensional ($\mathcal{P}$, $\mathcal{F}$) space shown in Fig. 3.

$$\mathcal{P} = \frac{\mathcal{W} - \mathcal{T}}{\mathcal{W} + \mathcal{T}} \quad , \quad \mathcal{F} = \frac{\mathcal{L} - \mathcal{W}}{\mathcal{L} + \mathcal{W}} \tag{23}$$

Values of $\mathcal{P}$ and $\mathcal{F}$ have a range of (0 - 1) whenever the inequality $\mathcal{L} \geq \mathcal{W} \geq \mathcal{T}$ is satisfied. When $\mathcal{L}$ reaches a substantial value compared to both $\mathcal{W}$ and $\mathcal{T}$, the filamentarity approaches unity. Then, the planarity of the object depends on the cross-section given by $\mathcal{T}$ and $\mathcal{W}$. When $\mathcal{W} \gg \mathcal{T}$, the planarity approximates unity and resulting in an infinitely long ribbon-shaped object $(\mathcal{P}, \mathcal{F}) \sim (1, 1)$. When $\mathcal{W} \sim \mathcal{T}$, the planarity approximates the zero value, resulting in circular cross-section and an object identified as an infinitely long tube $(\mathcal{P}, \mathcal{F}) \sim (0, 1)$. For a thin circular sheet, $(\mathcal{P}, \mathcal{F}) \sim (1, 0)$ where $\mathcal{W} \gg \mathcal{T}$ while $\mathcal{L} \sim \mathcal{W}$. For a perfectly spherical object, $\mathcal{L} = \mathcal{W} = \mathcal{T}$, the shapefinders are $(\mathcal{P}, \mathcal{F}) \sim (0, 0)$.

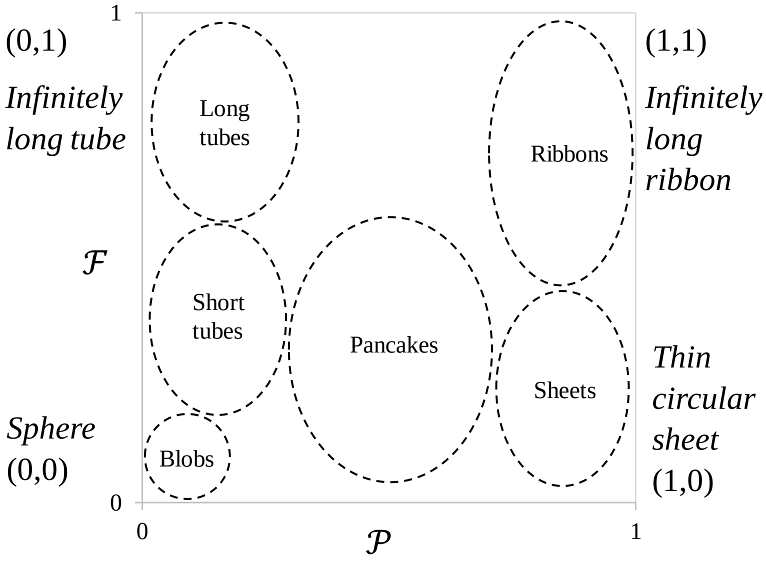

Figure 3: Typical regions for various simple shapes in the $\mathcal{P}$ - $\mathcal{F}$, shapefinders, plane [56].

The interest of this study is to investigate the morphology and structure of developing-flame and turbulence-flame interactions occurring at "intense reaction zones" of the flame front. Intense reaction zones refer to the regions of the reaction zone's layer, where fuel is being consumed at a very high rate (having a large value of $\dot{\omega}^*_{H_2}$). In this study, the threshold of defining and extracting the intense reaction zones is $\dot{\omega}^*_{H_2}$=0.9. This value is chosen to maximize the number of extracted reaction zones as it does not influence the results of the study. As shown in the supplementary document, intense reaction zones were extracted at multiple values of $\dot{\omega}^*_{H_2}$. The maximum number of extracted intense reaction zones was available at $\dot{\omega}^*_{H_2}$=0.9, and the obtained correlations with the turbulence statistics (to be discussed in Section 3.3) did not vary within multiple values of $\dot{\omega}^*_{H_2}$ [8, 9]. Intense reaction zones were extracted as flames propagated for mean turbulent flame radii, $r_{f,t}$ of 2 to 5 mm with an interval of 0.5 mm. As shown in the supplementary document, the effects of initial conditions diminished within this range. Therefore, flames are not subjected to strong transient effects due to ignition process. Furthermore, selected threshold was different compared to the study of Minamoto et al. [9] which is reasoned to the difference in the flame's configuration. In the current study, developing-flames are progressively expanding until they propagated out of the computational domain. That limited available data to the transition period from the ignition process until flames went out of the computational domain's bounds without reaching a final statistical state.

2.5 Turbulence statistics of reaction zones

To investigate the influence of turbulence on the morphology of flame and its reaction zone, the following averaging/sampling procedure for any chosen quantity q is applied [8, 9]. The density weighted volume averaged value, $[q]$ within the volume of an extracted object, V_Ω is computed as in Eq. (24).

$$[q] = \int_{V_\Omega} \rho q\left(\mathbf{x}\right) dV_\Omega / \int_{V_\Omega} \rho dV_\Omega \tag{24}$$

This procedure corresponds to a top-hat spatial filtering operation of a quantity q over a skewed volume, V_Ω within the reaction zones of interest. Each sampling volume, V_Ω is advected at its mean velocity $[u]$. Thus, any quantity $[q]$ is constructed within each extracted reaction zone. Accordingly, turbulence length and velocity scales were obtained within each sampling volume, V_Ω (local reaction zone) using Eq. (24) as in Eqs. (25–29).

$$\lambda^* = \frac{1}{3}\sum_{i=1}^{3}\sqrt{\left[u_i'^2\right] / \left[\left(\partial u_i'/\partial x_i\right)^2\right]} \tag{25}$$

$$\eta^* = \left(\left[\nu\right]^3 / \left[\varepsilon\right]\right)^{1/4} \tag{26}$$

$$\varepsilon = 2\left[\nu\left(S_{ij}S_{ij} - S_{ii}S_{ii}/3\right)\right] \tag{27}$$

$$u'_i = u_i - [u_i] \quad , \quad u'^{*} = \left(\left[(u_i - [u_i])^2\right]/3\right)^{1/2} \tag{28}$$

$$u_\eta{}^{*} = ([\nu]\,[\varepsilon])^{1/4} \tag{29}$$

where the symbol notations are the same as introduced in Section 2.2 and S_{ij} is the turbulent strain rate tensor. From above, Taylor microscale Reynolds number at intense reaction zones can be obtained as in Eq. (30).

$$Re_\lambda^{*} = [\lambda^{*}][u'^{*}]/[\nu] \tag{30}$$

Although V_Ω varies across the extracted samples, the averaged value obtained by Eq. (24) is a representation of a physical quantity q which each extracted reaction zone Ω has been exposed to. The same applies for the quantities obtained based on $[q]$ in Eqs. (25–30). The "*" is used to avoid confusing turbulence scales and intensities of intense reaction zones (will be referred to as "local") with "global quantities" of the turbulent field for each computed case.

3 Results and discussion

3.1 General flame features

Flames C1, C2, and C3 have propagated until they reached a mean turbulent flame radius, $r_{f,t}$ of 5 mm. As for flame T1, due to large scale turbulent motions, it was pushed from the center of the domain towards the $(-X, +Y)$ direction during propagation. Therefore, it is simulated to a mean turbulent flame radius, $r_{f,t}$ of 4 mm before going out of computational domain boundary. In parallel, non-reactive computations were performed to evaluate the decay in the turbulent kinetic energy of the turbulence fields for the four cases. The maximum observed decay in turbulence scales was 30% by comparison to the initial values, which should not present any qualitative change to the results of the study.

In Fig. 4, the flame fronts for current cases represented by 1350 K isotherms and coloured with Y_{H_2} and representative central slices of temperature, T fuel reaction rate, $\dot{\omega}_{H_2}$ and heat release rate, HRR are shown at mean turbulent flame radius, $r_{f,t}$ of 4 mm. Soon after ignition, the spherical flames started to outwardly propagate and quickly developed perturb surfaces, due to turbulence-flame interactions, which got more complex as they propagated. It is, also, clear that flame front convolution increased as the combustion regime shifted from the corrugated flamelets regime to the thin reaction zone regime (top to bottom). For all investigated flames, $\dot{\omega}_{H_2}|_{max}$ and HRR_{max} occurred at flamelets with highly negative curvatures. For premixed turbulent hydrocarbon flames, the largest fuel consumption rate values are observed at the negatively/positively curved flamelets depending on fuel type and its quality [17, 61, 62, 63, 64, 65]. As for lean hydrogen flames, the largest fuel consumption rate values occur at the positively curved flamelets [25, 66]. Here, despite the focusing of hydrogen at the positively curved flamelets, the difference in the location of intense burning was due to the relative richness of the stoichiometric hydrogen flames compared to the typically investigated lean hydrogen flame, which is reflected in both Lewis and Markstein numbers of the mixture ($Le_{eff} > 1$, $Ma > 0$). It is also noticed that for flame T1, absolute values of local fuel consumption rate significantly increased compared to the other three cases, which is related to the rapid change in species concentrations caused by small–scale turbulent motions, and is influencing transport rates ahead of flame front [27, 67, 68]. Therefore, affecting the molecular diffusivities of fuel, oxidizer, and present radicals in the flow field as the thermo-diffusive effects becomes evident in flame front formation [69].

To understand the physics and chemistry of stoichiometric hydrogen flames, Fig. 5 shows the joint pdfs of fuel consumption rate, heat release rate, tangential strain rate, the local concentration of H_2 and OH, and the local Lewis number of H_2 with the flame front's local curvature for flames C1 and T1 and at $r_{f,t}$ of 4 mm. It is clear from the negative correlations that the fuel's most significant consumption rates and heat release rates were occurring at the, highly strained, negatively curved flamelets of the flame front [24], which stemmed from the combination of flame stretching effects (Ma>0) of the spherical flames with positive mean curvature [65, 15], and the strong thermo-diffusive effects ($Le_{eff} > 1, Le_{H2} \ll 1$) for

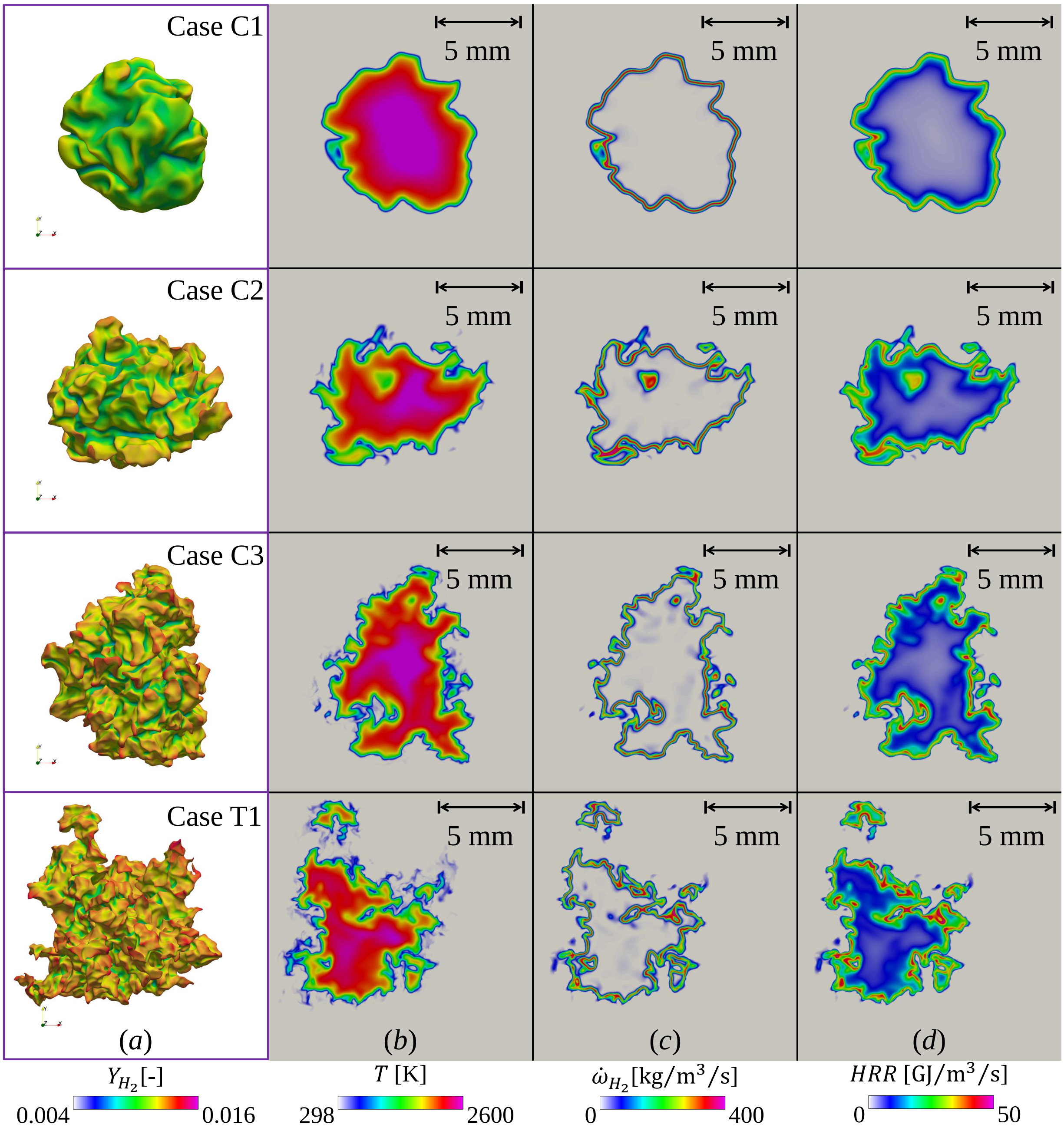

Figure 4: (a) Flame fronts represented by 1350 K isotherms (in violet frames) and coloured with Y_{H_2} and representative central slices of (b) temperature, T (c) fuel reaction rate, $\dot{\omega}_{H_2}$ and (d) heat release rate, HRR at mean turbulent flame radius, $r_{f,t}$ of 4 mm for current cases. Each property's range is unified for all cases. Dimension of each sub-figure is 16 × 16 mm.

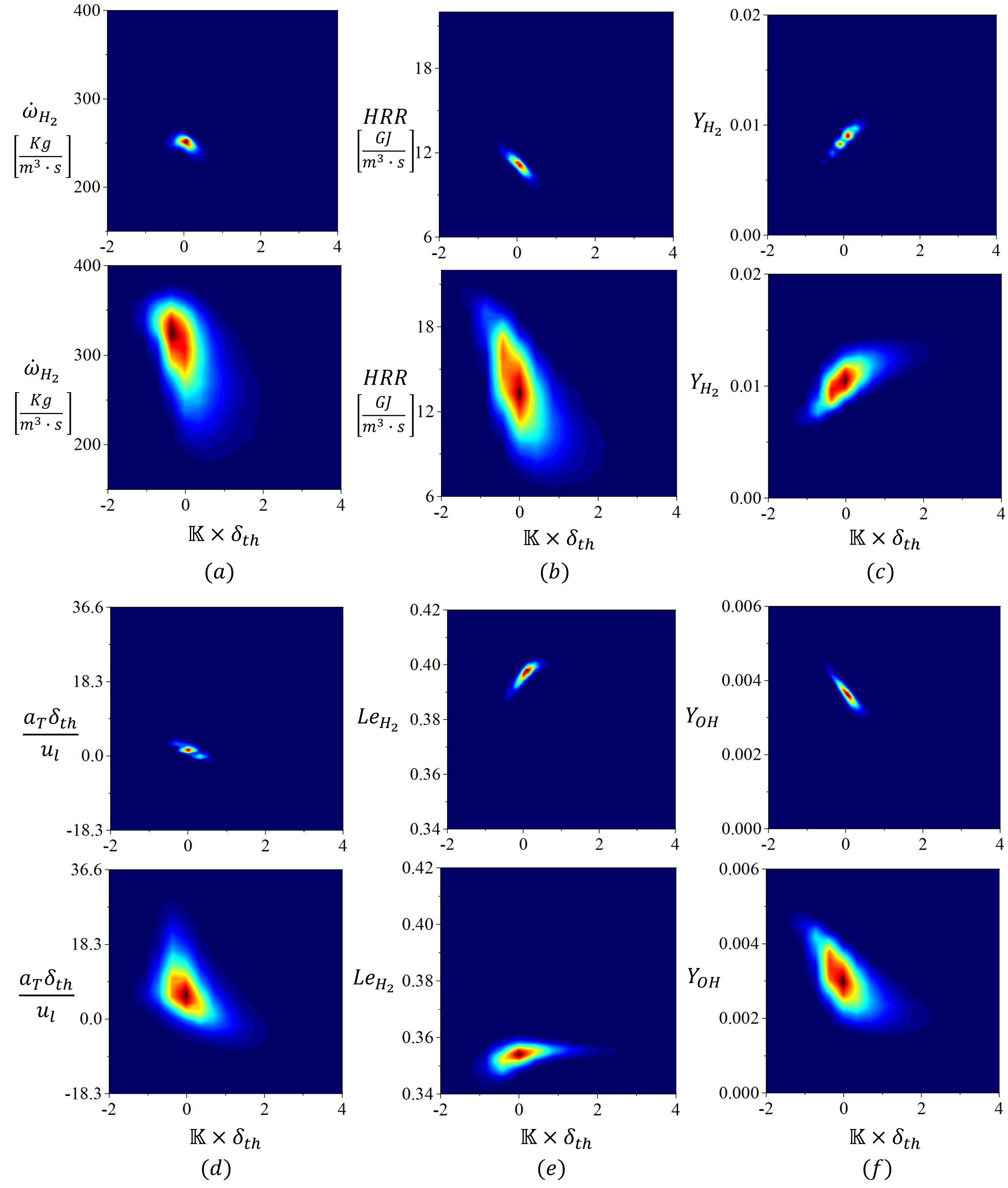

Figure 5: Joint pdf of (a) fuel consumption rate, (b) heat release rate, (c) local concentration of H_2, (d) tangential strain rate, (e) local Lewis number of H_2, (f) local concentration of OH with flame front's local curvature of flames C1 (upper row) and T1 (lower row) at $r_{f,t} = 4$ mm.

current stoichiometric hydrogen-air mixtures [66, 69, 70]. Since $Le_{H2} \ll 1$, the focusing of H_2 at the positively curved flamelets occurred faster than the defocusing of heat, resulting in simultaneous high fuel concentration and high temperature at the positively curved flamelets. The opposite was occurring at the negatively curved flamelets [24]. However, the burning of H_2 at the flame front is controlled by the concentrations of the OH radicals based on the elementary reaction ($H_2 + OH = H_2O + H$) in the detailed mechanism. Since Y_{OH} was larger (smaller) at the negatively (positively) curved flamelets, H_2 burned at a larger (smaller) rate, resulting in the observed profiles for fuel consumption rate and heat release rate. In turn, the concentration of OH radicals depended on the concentration of H radicals and O_2 based on the elementary reaction ($H + O_2 = OH + O$), where Y_{OH}, Y_H, and Y_{O_2} had similar profiles. Mentioned observations became possible with the combined utilization of detailed chemistry and detailed diffusion, which are not available in computations with single-step chemistry and/or fixed Lewis number strategy for involved species.

Since investigated flames have a non-unity Lewis number, the Huygen's propagation effects were prominent [71], where as the negatively curved flamelets propagated, their local areas were destroyed. That is confirmed by the lack of high negative value of the local curvature at the flame front. On the other hand, the positively curved flamelets continually propagated as they interacted with turbulent eddies, resulting in an increase in the local curvature and the associated flame stretch, leading to a sustained and robust propagation [17]. By examining the three-dimensional topology of the flame front, as turbulence level increased (larger Ka), the tendency to have detached flame structures increased as well, as seen in Fig. 6. This phenomenon was experimentally observed in [70] for lean hydrogen spherical flames, where it was attributed it to the occurrence of local extinction, just after forming a finger-like structure that bulges into the unburned mixture due to the difference in flame speed between positively and negatively curved flamelets and the associated difference in flame stretch. In current flames, for negatively curved flamelets which were formed on a thin bulging structure, the flame area destruction occurred in the form of local extinction, separating the bulging structure to become a detached flame structure. Smaller detached flame structures were not sustained, while larger ones, dominantly positively curved and having high fuel concentrations, expanded at low speeds while consuming the surrounding unburned mixture, until the main larger body of the flame caught up with them.

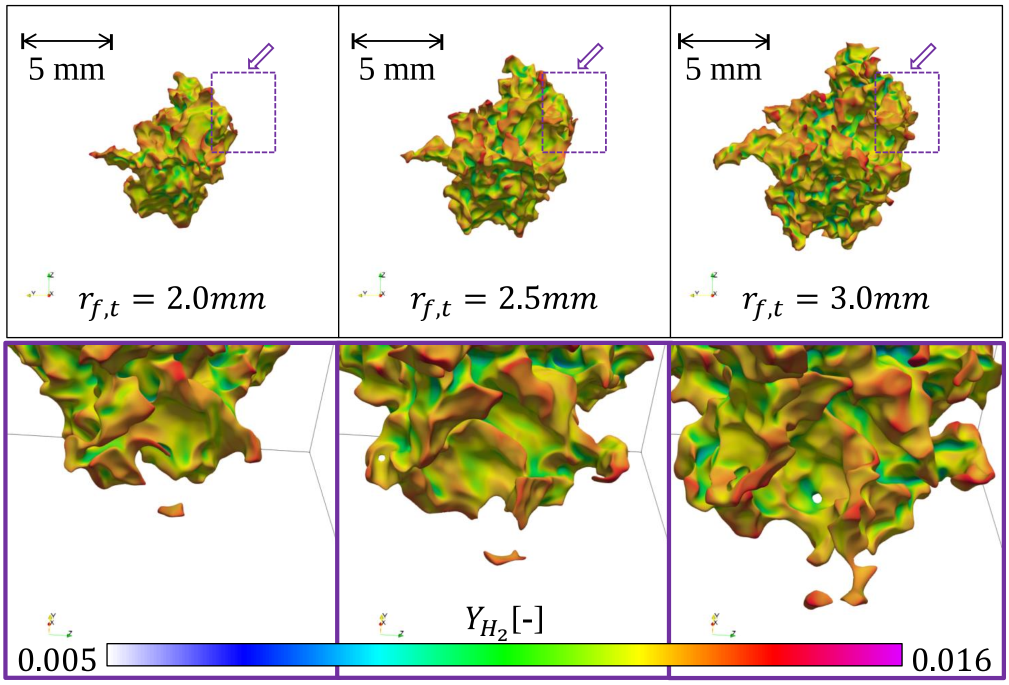

Figure 6: Flame front of flame T1, within $r_{f,t}$ range of 2.0 - 3.0 mm (upper panels), showing a detached flame structure (lower panels) viewed from slanted arrows' direction. Flame fronts are represented by 1350 K isotherms and coloured by Y_{H_2} with a unified scale.

The development of the normalized turbulent flame front area and normalized turbulent burning velocity is presented in Fig. 7(a). The area of turbulent flame fronts, A_t and turbulent burning velocities, u_t were normalized by the mean turbulent flame front area and unstretched laminar burning velocity (u_l=1.97 m/s), respectively. Here, the mean turbulent flame front area, A_l is the surface area of a sphere with the equivalent volume as the burned gas volume and contained within the turbulent flame front. In turn, this surface area is the same as the flame front area of a laminar flame with the same burned gas volume (having $r_{f,t} = r_f$) and is evaluated as $A_l = 4\pi {r_{f,t}}^2 = 4\pi {r_f}^2$. The turbulent flame front area's variation with turbulent burning velocity is shown in Fig. 7(b), while the variation of mean flame stretch, α with the burning velocities, u_n and u_t, is shown in Fig. 7(c). Here, mean flame stretch for turbulent flames is obtained using Eq. (13). As turbulence level increased (larger Ka), local small scale mixing of unburned mixture ahead of the flame front increased [27], resulting in the sharp

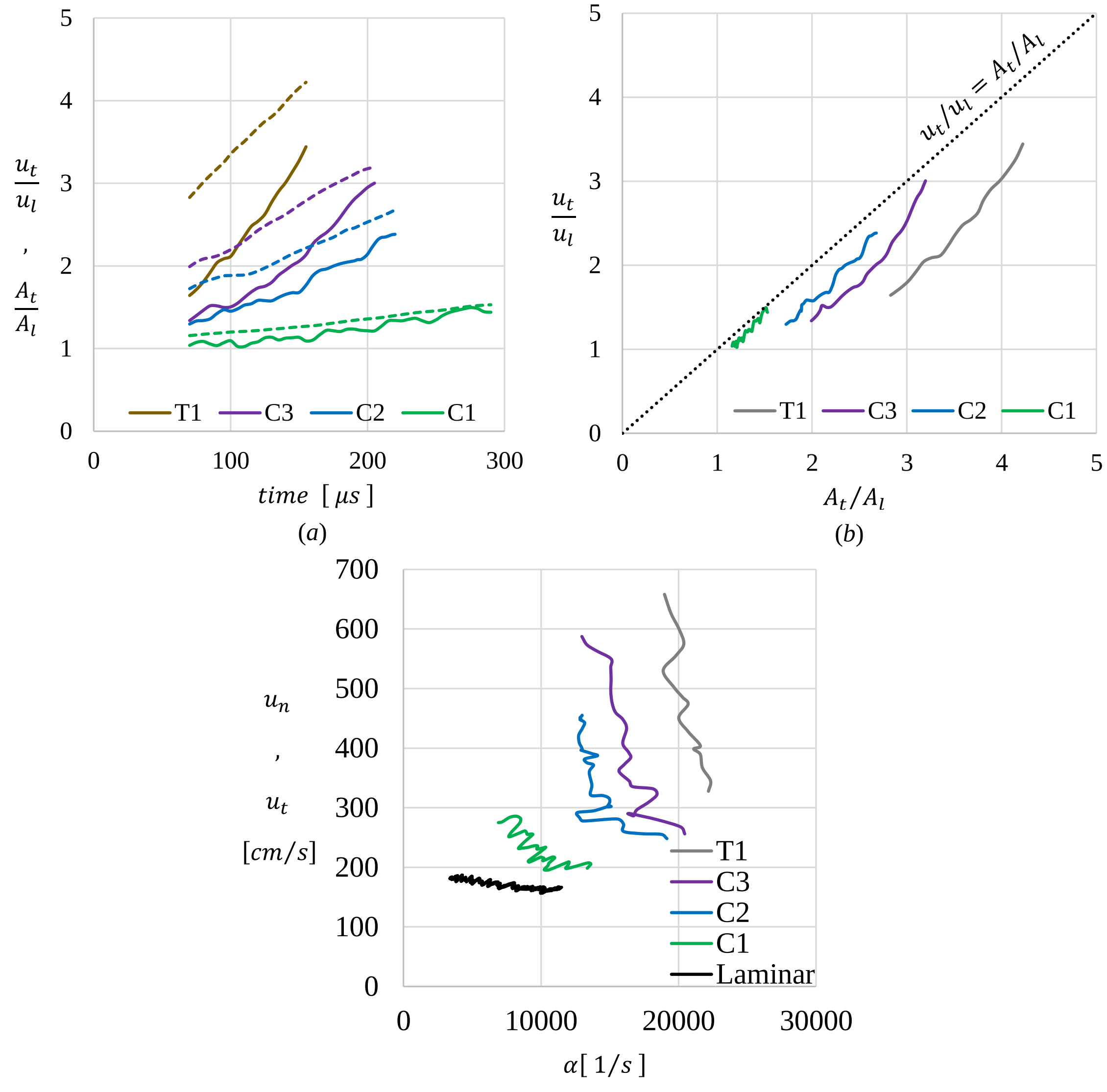

(c)

Figure 7: Time history of (a) $u_t \setminus u_l$ (solid lines) and $A_t \setminus A_l$ (dashed lines), variation in (b) $A_t \setminus A_l$ against $u_t \setminus u_l$, and variation in (c) α against u_n and u_t.

rise in burning velocities. Despite that, the ratio (u_t/u_l) was smaller than the ratio (A_t/A_l). Furthermore, an apparent increase in the deviation from the line $[(u_t/u_l) = (A_t/A_l)]$ is seen as the combustion shifted towards the thin reaction zones regime. That is attributed to the increase in turbulent stretching effects with the increase in turbulence intensity [72]. Spherical flames have mean positive curvatures, where positively curved flamelets were subjected to weak tangential strain rates (Fig. 5(d)). The local implication of that was the reduction in the burning intensity at the dominant positively-curved flamelets [24], resulted in a decrease in the overall burning velocity, u_t/u_l compared to the overall increase in the area, A_t/A_l. The opposite to that would be observed for spherical flames with $Le \ll 1$ [70], where the intense burning occurs at the positively curved flamelets, significantly increasing the burning velocity and collectively increasing the flame front area by interacting with the turbulent eddies. Then, the larger flame front becomes more positively curved than negatively curved, which would be followed by an intensified burning at the positively curved flamelets, leading to a repeat in the mentioned cycle, and having $(u_t/u_l) > (A_t/A_l)$ [24, 15, 73]. Therefore, depending on the Lewis number, a different balance between the flame's thermo-diffusive characteristic and flame stretch contribution (due to turbulence-flame interactions and reflected in the curvature, strain, and Markstein number) is sustained to propagate the spherical flame. Also, it appears that despite having $Le_{H2} \ll 1$, which significantly influenced the concentration profile of the fuel, the global behaviour of the flames was dominantly controlled by Ma and Le_{eff}. That being said, employing the detailed diffusion, where estimating the molecular diffusivity and diffusion velocity of involved species was more accurate, revealed the local changes in the concentrations of involved species across the investigated turbulent cases and their effects on the local chemistry and heat release rate profiles, which would be focused on in upcoming works.

3.2 Characteristic scales of intense reaction zones

Figure 8 presents a sample of normalized reaction isosurfaces of computed cases. The grey isosurface holds the threshold of $\dot{\omega}^*_{H_2} = 0.5$, which can represent the overall reaction zone shape, while the red isosurface holds the threshold of $\dot{\omega}^*_{H_2} = 0.9$, which represents intense reaction zones. At mean turbulent flame radius, $r_{f,t}$ of 4 mm, the total volume of the reaction layer for the turbulent flames to the total volume of the reaction layer for the laminar flame (at $\dot{\omega}^*_{H_2}$=0.5) is 1.15 times, 1.65 times, 1.71 times, and 2.94 times for flames C1, C2, C3, and T1, respectively. Furthermore, compared to the laminar flame, the volumetric fraction of intense reaction zones at $\dot{\omega}^*_{H_2}$=0.9 per the overall reaction layer at $\dot{\omega}^*_{H_2}$=0.5 is 0.14% (flame C1), 1.66% (flame C2), 1.71% (flame C3) and 2.58% (flame T1). In a way, that can be seen as an extension of the boundaries of intense reaction zones of the turbulent flames, especially once the strong influence of the turbulent flame stretch is considered.

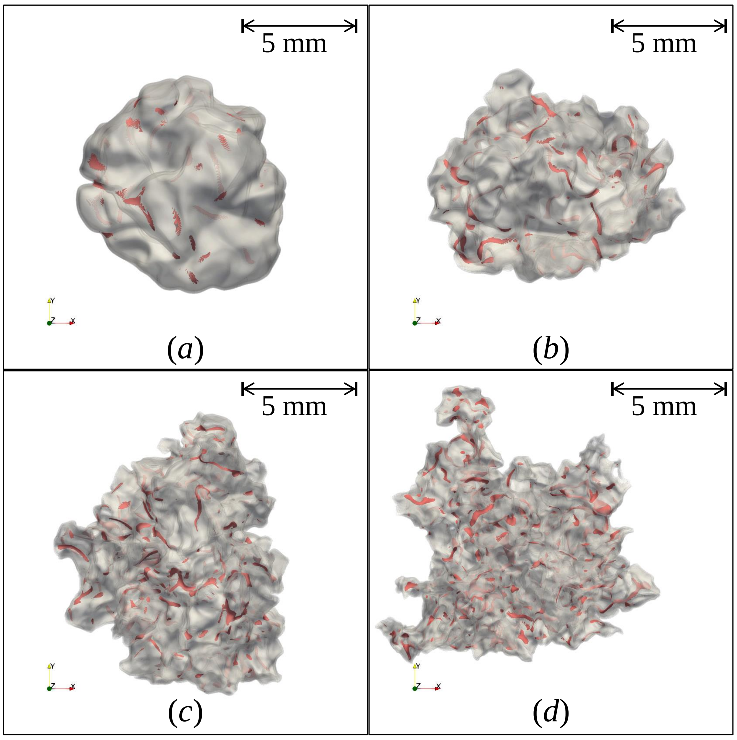

Figure 8: Instantaneous reaction rate iso-surfaces at $r_{f,t}$=4 mm, for C1 (a), C2 (b), C3 (c) and T1 (d). In transparent grey: $\dot{\omega}^*_{H_2}$=0.5. In red: $\dot{\omega}^*_{H_2}$=0.9.

Using the shapefinders, extracted intense reaction zones were analyzed based on the Minkowski functionals. Extracted intense reaction zones contained, on an average, 500-1000 mesh points. That was deemed sufficient to compute turbulence statistics for each intense reaction zone and provide a meaningful understanding of initial flame structure and morphology. However, some extracted intense reaction zones had many holes within them which could compromise statistics calculation within the object depending on the number of holes in the object and the number of mesh points containing the object. To eliminate any subjectivity in the present study, objects having G>1 were not used in obtaining statistics of this study. The distribution of the intense reaction zones in the ($\mathcal{P}$ – $\mathcal{F}$) non-dimensional plane is presented in Fig. 9, while Fig. 10 shows a sample of them and their ($\mathcal{P}$, $\mathcal{F}$) values. While presented samples do not statistically represent the entire range of intense reaction zones' shape, they can provide a visual understanding of ($\mathcal{P}$, $\mathcal{F}$) values for different shapes. Intense reaction zones for flame C1 were mostly classified as thick short tubes (Fig. 10(a)), while some had very small surface area and thin pancake shapes at larger $r_{f,t}$ (Fig. 10(b)). On an average, reaction zones of flames C2, C3 and T1 had similar geometrical shapes and were mostly classified as pancakes with various thicknesses, surface areas, and complexities (Fig. 10(c-g)). A distinct difference for flame T1 was the frequent formation of reaction zones with complex geometry at larger $r_{f,t}$ (Fig. 10(h)).

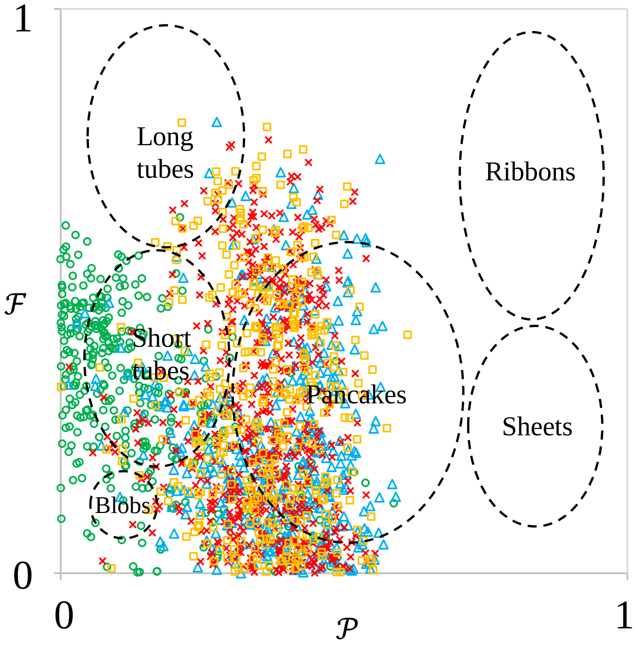

Figure 9: Shapefinders, $\mathcal{P}$ and $\mathcal{F}$, for case C1 (green circle), C2 (blue triangle), C3 (red diamond) and T1 (orange square).

Table 2 summarize statistics of extracted intense reaction zones, while Fig. 11 provides the population distribution of the characteristic scales ($\mathcal{T}$, $\mathcal{W}$, and $\mathcal{L}$) and shapefinders ($\mathcal{P}$ and $\mathcal{F}$) of extracted intense reaction zones. As each flame propagated, the number of extracted intense reaction zones (extracted objects, N) has increased. For example, for flame C3, N was 11, 23, 61, 83, 107, 143, and 168 at $r_{f,t}$ of 2.0, 2.5, 3.0, 3.5, 4.0, 4.5, and 5.0 mm, respectively. As the turbulent combustion regime shifts from the corrugated flamelets towards the thin reaction zones regime, there was an increase in the total fuel burning rate, which is indicated here by the broadening of the boundaries of intense reaction zones (larger mean $\mathcal{W}$ and $\mathcal{L}$ at larger Ka) and forming new ones (larger N at larger Ka) at the flame front.

Table 2: Statistical summary of extracted objects. Showing number of extracted objects, N, mean $\mathcal{P}$, $\mathcal{F}$, $\mathcal{T}$, $\mathcal{W}$ and $\mathcal{L}$ of extracted objects with their standard deviation in brackets.

Case	N	$\mathcal{P}$	$\mathcal{F}$	$\mathcal{T}/\delta_{th}$	$\mathcal{W}/\delta_{th}$	$\mathcal{L}/\delta_{th}$
C1	361	$0.15_{(0.13)}$	$0.31_{(0.15)}$	$0.08_{(0.018)}$	$0.12_{(0.06)}$	$0.23_{(0.10)}$
C2	419	$0.38_{(0.11)}$	$0.24_{(0.17)}$	$0.11_{(0.021)}$	$0.26_{(0.08)}$	$0.48_{(0.30)}$
C3	596	$0.36_{(0.09)}$	$0.28_{(0.20)}$	$0.11_{(0.019)}$	$0.24_{(0.05)}$	$0.51_{(0.33)}$
T1	406	$0.36_{(0.10)}$	$0.31_{(0.20)}$	$0.13_{(0.024)}$	$0.27_{(0.07)}$	$0.62_{(0.40)}$

As turbulence level increased (larger Ka), intense reaction zones got thicker (also seen through mean values in Table 2). Depending on local length scales and intensities of mixing processes at the flame front, broader/faster transport of heat and radical, towards the unburned mixture occurred, resulting in the observed thickening of local reaction layers. Regarding the topology of flames C2, C3, and T1, it is noticed that the majority of intense reaction zones had $\mathcal{L}$ values that were comparable to $\mathcal{W}$ values. Despite that, many intense reaction zones had significantly large $\mathcal{L}$ values that increased its mean. Here, as turbulence level increased (larger Ka), number of intense reaction zones having a significantly large $\mathcal{L}$ value increased and were becoming more common at a larger mean turbulent flame radius.

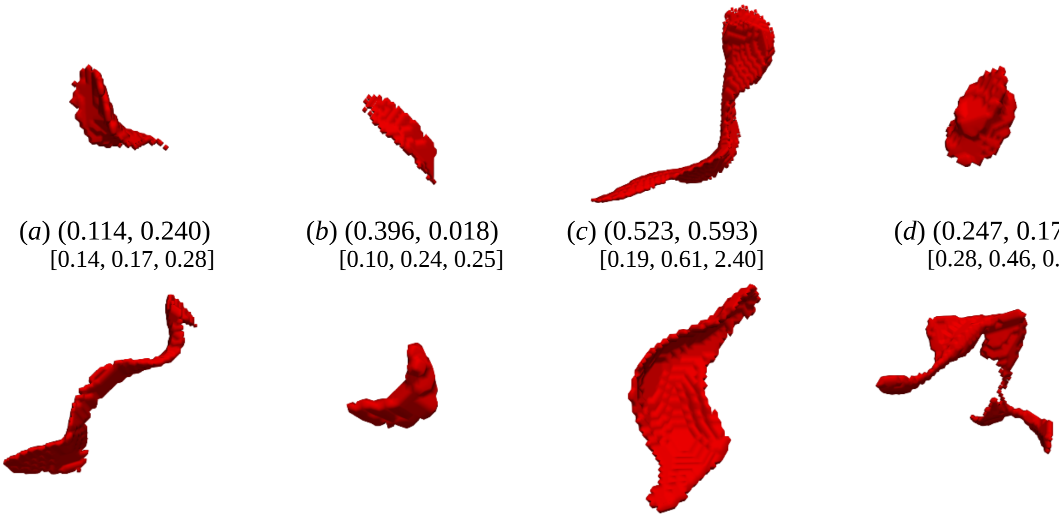

(*a*) (0.114, 0.240) [0.14, 0.17, 0.28]

(*b*) (0.396, 0.018) [0.10, 0.24, 0.25]

(*c*) (0.523, 0.593) [0.19, 0.61, 2.40]

(*d*) (0.247, 0.177) [0.28, 0.46, 0.65]

(*e*) (0.401, 0.704) [0.14, 0.33, 1.92]

(*f*) (0.135, 0.284) [0.18, 0.24, 0.43]

(*g*) (0.613, 0.422) [0.14, 0.58, 1.42]

(*h*) (0.214, 0.799) [0.18, 0.28, 2.50]

Figure 10: Samples of extracted reaction zones and their ($\mathcal{P}$, $\mathcal{F}$) and [$\mathcal{T}/\delta_{th}$, $\mathcal{W}/\delta_{th}$, $\mathcal{L}/\delta_{th}$] values for C1(a-b), C2 (c-d), C3 (e-f) and T1 (g-h).

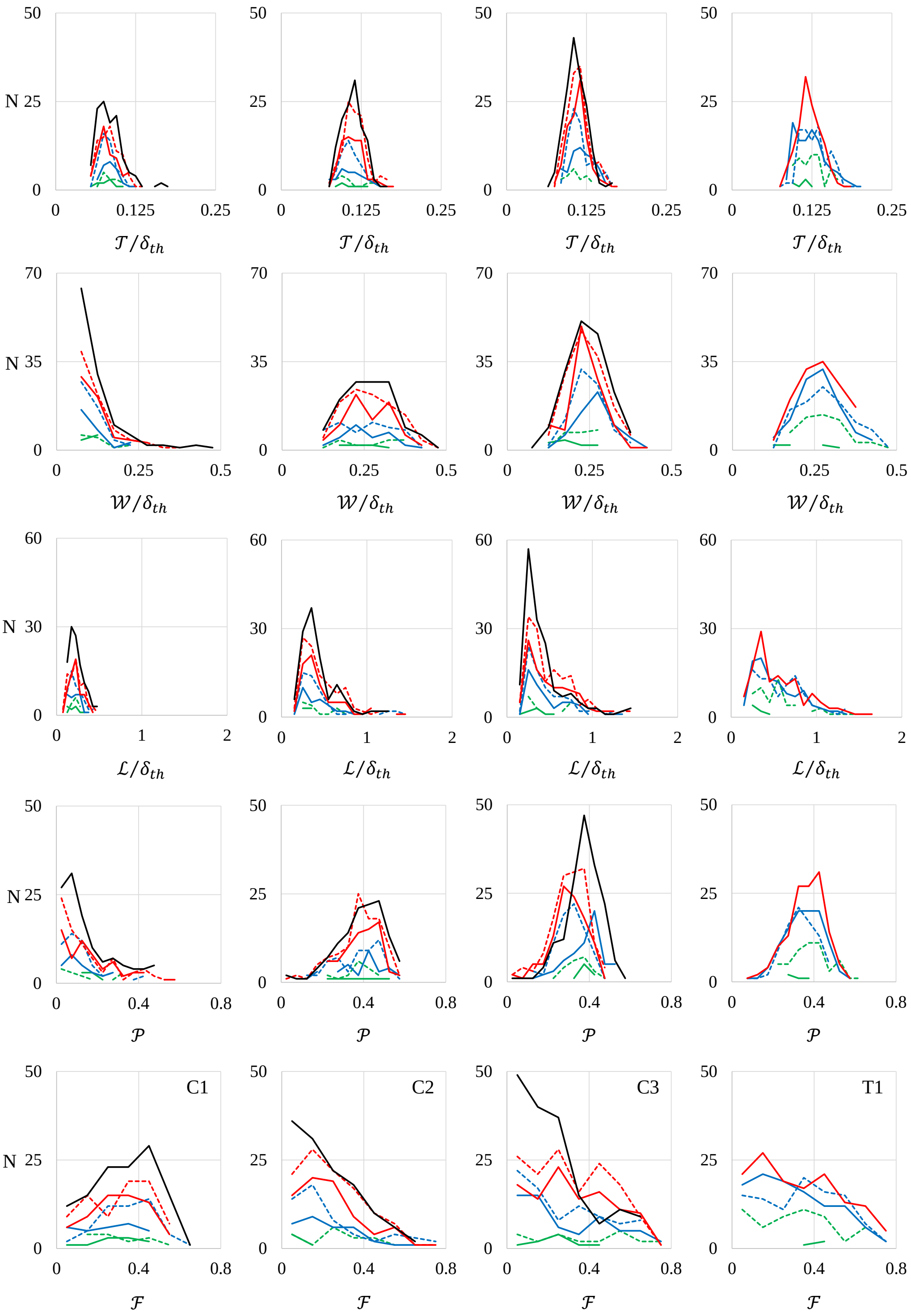

Figure 11: Distribution of intense reaction zones (N) with, $\mathcal{T}$, $\mathcal{W}$, $\mathcal{L}$, $\mathcal{P}$ and $\mathcal{F}$ for computed flames at $r_{f,t}$ = 2.0 mm (solid green), 2.5 mm (dashed green), 3.0 mm (solid blue), 3.5 mm (dashed blue), 4.0 mm (solid red), 4.5 mm (dashed red), and 5.0 mm (solid black).

Those “long” intense reaction zones resulted from strong turbulent motions and were highly strained (Fig. 5(d)). As for flame C1, most of its intense reaction zones had minimal $\mathcal{W}$ and $\mathcal{L}$ values, which is also clear through the means in Table 2. That helps to clarify the small volumetric fraction of intense reaction zones per overall reaction zones for case C1. The distribution and the mean of the three characteristic scales did not change for each investigated flame as it propagated (see the top of the bell for the distributions). That indicates the consistency in the geometry of local flame structures formed due to turbulence-flame interactions for each flame (at least within early stages of flame development). While the means remained unchanged, the increase in their distributions' skewness towards more significant values at larger flame sizes was due to the most substantial small-scale turbulent motions at each particular flame size, indicating to the possibility of shifting the distributions at later stages of flame development.

By considering Eq. (23), the planarity, $\mathcal{P}$ shapefinder gives a relative understanding to the changes between the thickness of intense reaction zones (here $\mathcal{T}$) and their topology (here $\mathcal{W}$). The filamentarity, on the other hand, holds information related to the topology/complexity of the local flame front as its value depends on the changes between the length, $\mathcal{L}$ and the width, $\mathcal{W}$ of intense reaction zone. The distribution of $\mathcal{P}$ was closely following the distribution of $\mathcal{W}$. As flames C2, C3, and T1 propagated, the increments of $\mathcal{W}$ were larger than the increments of $\mathcal{T}$, which indicates that the rate of increasing the surface area of local flame structures, due to stretching effects, was larger than the rate of thickening of those structures, leading to producing local flame structures with larger values of $\mathcal{P}$ over a wide range of thicknesses. As for their topology, intense reaction zones with smaller $\mathcal{F}$ value (comparable length and width) were dominant. However, many intense reaction zones had larger $\mathcal{F}$ due to the substantial increase in their $\mathcal{L}$, due to stretching effects, especially at larger Ka. As for flame C1, as it propagated, the dominant small values of $\mathcal{P}$ show that the local flame structures got thickened and stretched by a similar rate, while the different distribution of $\mathcal{F}$ was due to the wide gap between $\mathcal{W}$ and $\mathcal{L}$. It should be noted that larger $\mathcal{F}$ does not necessarily mean more surface area or higher flame front coverage. For flame C1, the small values of $\mathcal{W}$ and the absence of intense reaction zones with substantially larger $\mathcal{L}$, compared to the other three flames, led to the observed distinct distribution.

The geometry of intense reaction zones of spherical flames have some key differences compared to planar flames, which are related to (i) their sizes/volumes, (ii) their thicknesses, and (iii) their topologies. On average, the sizes of intense reaction zones for planar flames in [9] were 2-5 times larger than those for the spherical flames. That implies that the characteristic scales (geometrical extensions) of intense reaction zones for the planar flames were larger than those for the spherical flames, which is reasonable considering that planar flames are well-developed while spherical flames are still evolving. The development of local flame thickness of spherical flames is controlled by turbulent strain rates, while for planar flames it is controlled by self-propagation and dilatation [74], which implies that spherical flames got thicker as they evolved through turbulence-flames interactions (values of $\mathcal{T}$ are getting larger), while planar flames could reach a statistically stationary state in terms of its brush thickness (large values of $\mathcal{T}$ were achieved at steady state condition). Therefore, the gap between $\mathcal{W}$ and $\mathcal{T}$ for planar flame was small leading to a smaller mean of $\mathcal{P}$ [9], while the opposite would be occurring in spherical flames. While the surface area of intense reaction zones for spherical flames was very small (due to small flame size), its counterpart in the planar flame was much larger.That would increase the probability of having larger values of $\mathcal{F}$ for the planar flames while they were less encountered in the spherical flames. That being said, once spherical flames reach a later stage of their development, the topologies of intense reaction zones would be closer in resemblance to those of the planar flames. As for comparing the geometry of intense reaction zones with structures of decaying homogeneous isotropic turbulence, Leung et al. [56] have analysed enstrophy and dissipation structures and confirmed, through the Minkowski functionals and shapefinders, the development of their tubular shapes.

3.3 Local turbulence properties of intense reaction zones

In order to discuss the correlations between local turbulence properties and intense reaction zones, it is essential to clarify the relationship between the shapefinders and both of flame structure and morphology. Since planarity is the non-dimensional quantity to represent $\mathcal{T}$, it portrays the thickness of a three-dimensional object (reaction zone). Thus, it is correlated to the structure of the flame. On the other hand, the filamentarity is the non-dimensional quantity that describes the comparison between $\mathcal{W}$ and $\mathcal{L}$ of a three-dimensional object. Consequently, it characterizes surface/topology information. Hence, filamentarity is correlated with the flame's morphology. To find out which turbulence properties influenced flame morphology and structure under present conditions, the conditional averages of local Taylor microscale, λ^* and local turbulence intensity, u'^* conditioned with respect to $\mathcal{P}$ and $\mathcal{F}$ are shown in Fig. 12, while the conditional averages $\langle\lambda^*|\mathcal{T}\rangle$, $\langle\lambda^*|\mathcal{W}\rangle$, $\langle\lambda^*|\mathcal{L}\rangle$, $\langle u'^*|\mathcal{T}\rangle$, $\langle u'^*|\mathcal{W}\rangle$, $\langle u'^*|\mathcal{L}\rangle$, $\langle Re^*_\lambda|\mathcal{T}\rangle$, $\langle Re^*_\lambda|\mathcal{W}\rangle$, and $\langle Re^*_\lambda|\mathcal{L}\rangle$ are shown in Fig. 13. Furthermore, the conditional averages of local Kolmogorov length, η^* and local Kolmogorov velocity, $u_\eta{}^*$ scales conditioned with respect to $\mathcal{P}$ and $\mathcal{F}$ are shown in Fig. 14.

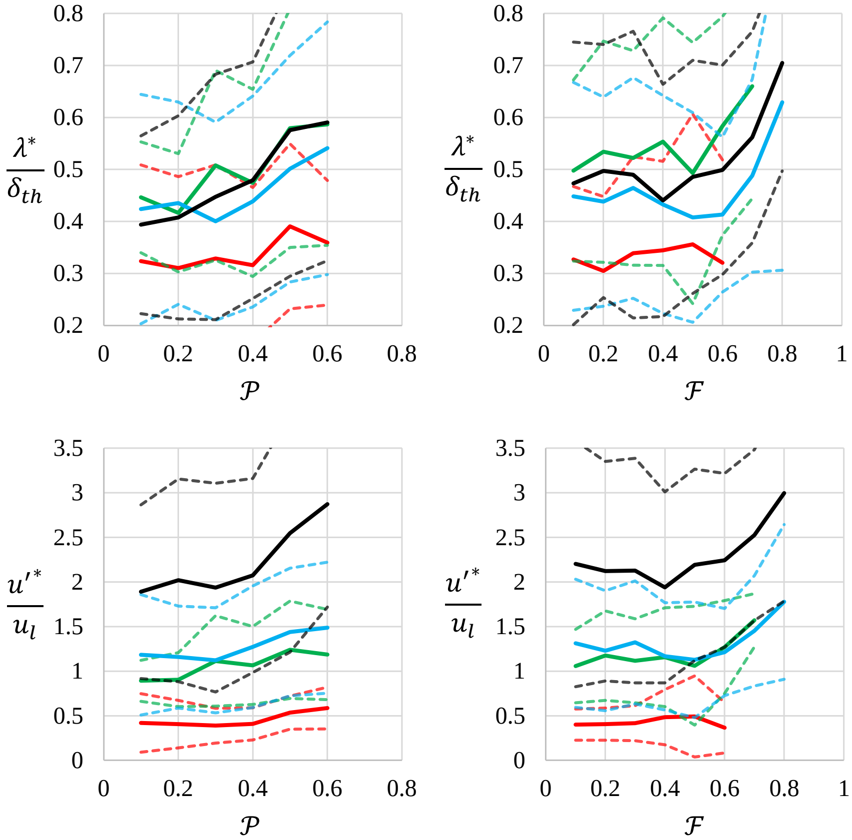

Figure 12: Mean (bold) and standard deviation (dashed) of conditional averages of local Taylor microscale, $\langle\lambda^*|\mathcal{P}\rangle$ and $\langle\lambda^*|\mathcal{F}\rangle$ and local turbulence intensity, $\langle u'^*|\mathcal{P}\rangle$ and $\langle u'^*|\mathcal{F}\rangle$ for flames C1 (red), C2 (green), C3 (blue) and T1 (black). Conditional averages are shown for bins containing more than ten samples.

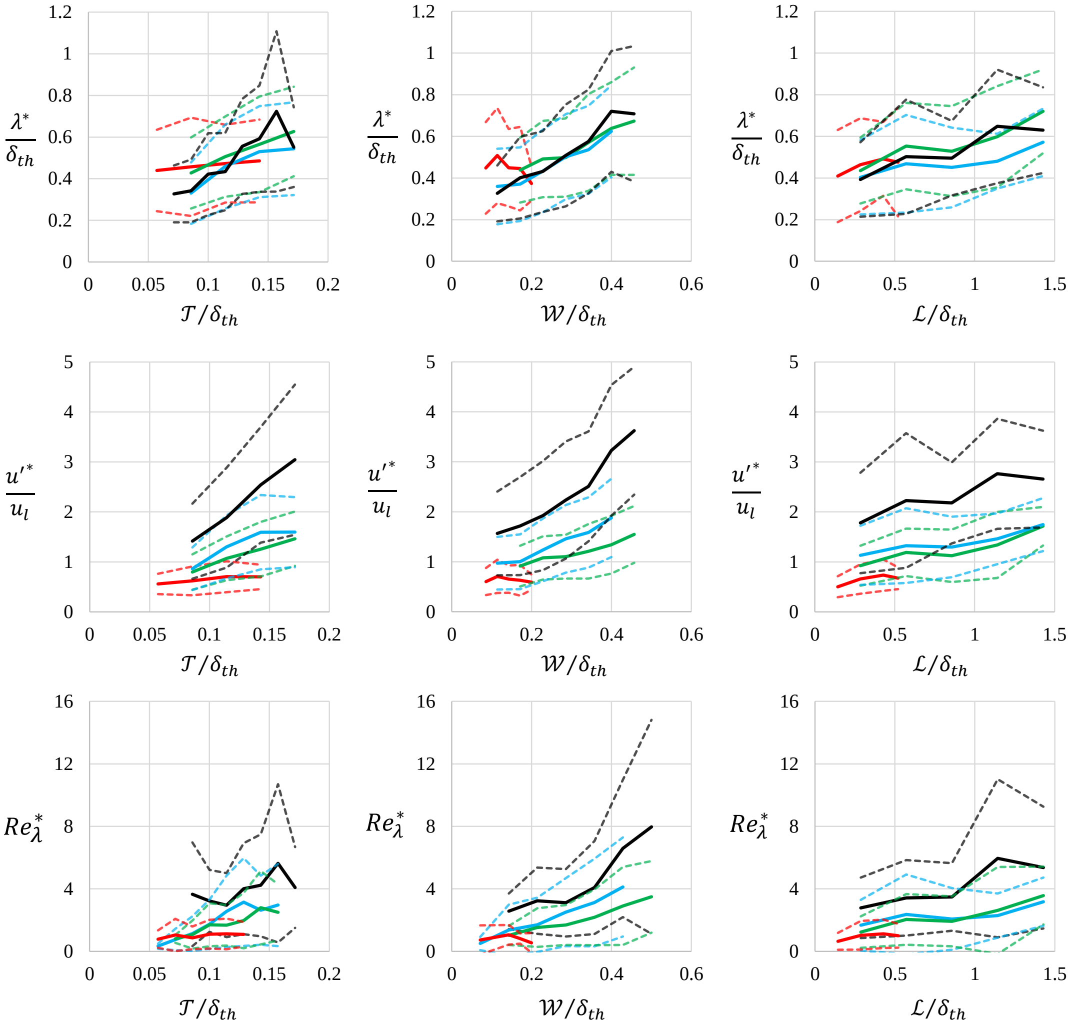

Figure 13: Mean (bold) and standard deviation (dashed) of conditional averages of local Taylor microscale, $\langle \lambda^* | \mathcal{T} \rangle$, $\langle \lambda^* | \mathcal{W} \rangle$, and $\langle \lambda^* | \mathcal{L} \rangle$, local turbulence intensity, $\langle u'^* | \mathcal{T} \rangle$, $\langle u'^* | \mathcal{W} \rangle$, and $\langle u'^* | \mathcal{L} \rangle$, and local Taylor microscale Reynolds number $\langle Re_\lambda^* | \mathcal{T} \rangle$, $\langle Re_\lambda^* | \mathcal{W} \rangle$, and $\langle Re_\lambda^* | \mathcal{L} \rangle$ for flames C1 (red), C2 (green), C3 (blue) and T1 (black). Conditional averages are shown for bins containing more than ten samples.

The conditional averages, $\langle \lambda^* | \mathcal{P} \rangle$, $\langle u'^* | \mathcal{P} \rangle$, $\langle \lambda^* | \mathcal{F} \rangle$, and $\langle u'^* | \mathcal{F} \rangle$, suggest that an eddy with larger λ^* yield "thinner and broader" reaction zones (having larger $\mathcal{W}$ and significantly smaller $\mathcal{T}$) as well as more "flame front coverage" (as $\mathcal{L}$ gets very large compared to the already large $\mathcal{W}$), conditioned to larger u'^* intensities. ~~That indicates to the potency of the induced flame stretch as the Taylor microscale is the strain rate length scale, which is also clear in Fig. 13 through the increasing gap between $\mathcal{L}$ and $\mathcal{W}$ at larger λ^*.~~ That indicates the potency of the induced flame stretch on the reaction zones, especially while considering

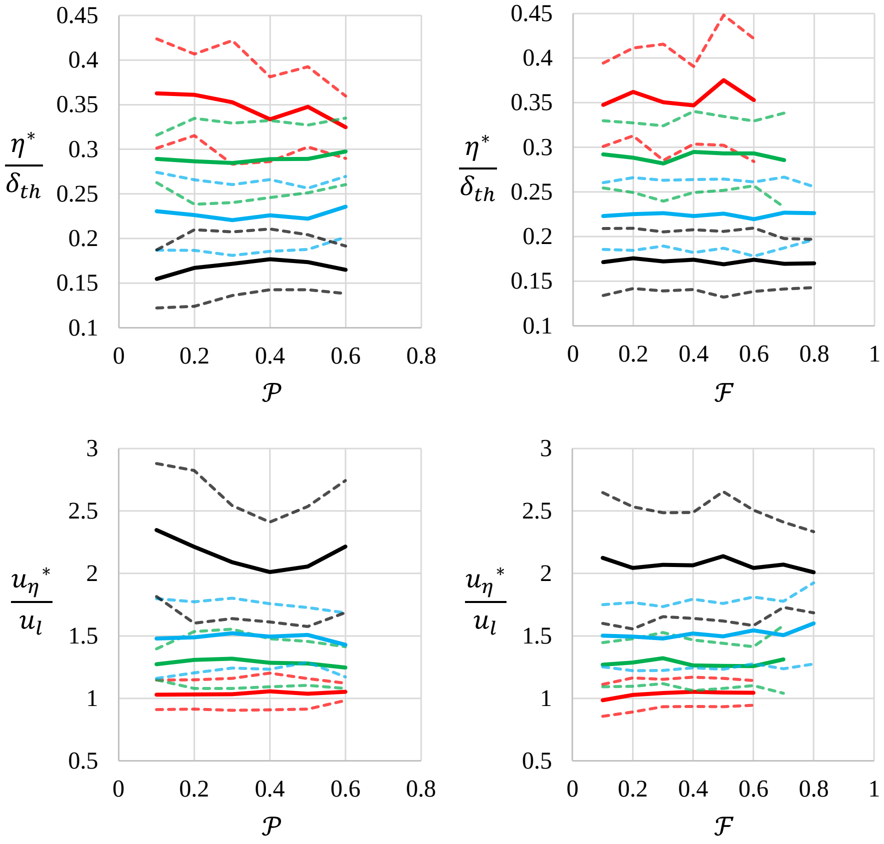

Figure 14: Mean (bold) and standard deviation (dashed) of conditional averages of local Kolmogorov length scale, $\langle \eta^* | \mathcal{P} \rangle$ and $\langle \eta^* | \mathcal{F} \rangle$ and local Kolmogorov velocity scale, $\langle u_\eta{}^* | \mathcal{P} \rangle$ and $\langle u_\eta{}^* | \mathcal{F} \rangle$ for flames C1 (red), C2 (green), C3 (blue) and T1 (black). Conditional averages are shown for bins containing more than ten samples.

the increasing gap between $\mathcal{L}$ and $\mathcal{W}$ at larger λ^* in Fig. 13. The induced flame stretch on intense reaction zones resulted from the combination of propagation under high negative curvature and straining effects characterized with λ^* and u'^* which vary over a wide range across the reaction zones. The physical interpretation of the Taylor microscale in this context is based on its definition as the velocity gradient of the flow, which justifies using it as a length scale for flow straining and turbulent stretching [72]. As for flame C1, although turbulent motions can be comparable in their λ^* sizes to the other flames, the local intensities of u'^* associating those motions were very weak. Hence, those turbulent motions lightly strained the flame front (Fig. 5-d), which did not strongly influence the flame front morphology, and accordingly, they are weakly correlated with $\mathcal{P}$ and $\mathcal{F}$. ~~which would also explain~~ That also explains the hardly wrinkled flame front of flame C1 as well as its relatively slow propagation rate. Therefore, with sufficiently large turbulence intensities, turbulent motions with length scales of Taylor microscale influenced flame morphology directly. At the same time, they modified the local flame structure through thickening and preheat zone structure through broader/faster scalar transport operations normal to the flame front of developing-flame, which would indirectly influence the flame's morphology. ~~Here, it is important to keep in mind the physical interpretation of the Taylor microscale based on its definition as the velocity gradient of the flow, which justifies using it as a length scale for flow straining and turbulent stretching [72].~~

Minamoto et al. [9] have investigated several planar flames, and directly correlated the topology of local reaction zones with turbulent fluctuations having a length scale larger than the Taylor microscale size. On the other hand, they found a weak correlation between Taylor microscale size's turbulent motions and the development of the flame's structure, which contrasts with the current study's findings. Since the configuration of planar flames allow for a long flame evolution time where they can reach their fully-developed state [75], the flame structure is controlled by self-propagation of the wrinkled flame front and by dilatation, while the strain rate effect on their mean flame structure is insignificant as it got counterbalanced by the curvature contributions [74]. However, current flames were spherically expanding flames with a developing-flame front and their structure and burning velocities could be significantly affected by flame stretch [74, 14], as seen in the stronger correlations in $\langle \lambda^* | \mathcal{P} \rangle$, $\langle u'^* | \mathcal{P} \rangle$, $\langle \lambda^* | \mathcal{T} \rangle$, and $\langle u'^* | \mathcal{T} \rangle$. Furthermore, considered flames were positively "curved flames" in general, even if there were "locally" compressed parts in the flames (negative curvature). Therefore, combined instantaneous influences of curvature and strain rates would significantly contribute to flame structure development. As for the evolution of flame front morphology, for planar, spherical, and swirl flames, turbulent eddies of Taylor microscale sizes and larger would have a substantial contribution to the development of their flame front morphology through the exerted strain rates [8, 9].

The conditional averages $\langle Re^*_\lambda | \mathcal{T} \rangle$, $\langle Re^*_\lambda | \mathcal{W} \rangle$, and $\langle Re^*_\lambda | \mathcal{L} \rangle$ give a unique insight towards turbulence statistics at the flame front, as they show the dissidence between global ones representing the turbulence of investigated cases and local ones representing the interactions at flame front. The obvious reason for the huge drop in Re^*_λ compared to Re_λ can be attributed to turbulence decay leading to lower values of u'^* at the flame front. However, that did not explain the observed tendencies in $\langle\lambda^*|\mathcal{T}\rangle$, $\langle\lambda^*|\mathcal{W}\rangle$, and $\langle\lambda^*|\mathcal{L}\rangle$ as the mean and deviations of λ^* at each value of the characteristic scales were within a close range despite the ~~many~~ differences in turbulence length and velocity scales within the computed cases. Although λ had a wide range across the computed conditions, the variation in λ^* was limited and correlated with ~~dependant on~~ the local geometrical scales of the flame front. As seen in Fig. 11, the probability of having intense reaction zones with larger geometrical length scales was higher at larger flame sizes (larger $\mathcal{W}$ and $\mathcal{L}$ at larger $r_{f,t}$). Therefore, it is reasonable to induce that λ^* here is (i) a length scale representing turbulence-flame interactions at which effective wrinkling or local straining/stretching of the flame front occurred, (ii) is dependant on the size of the developing flame ($r_{f,t}$), and (iii) is irrespective of eddies with larger/smaller length scales in the flow field. However, as seen in $\langle u'^*|\mathcal{T}\rangle$, $\langle u'^*|\mathcal{W}\rangle$, and $\langle u'^*|\mathcal{L}\rangle$, the effective wrinkling speed was controlled by u'^*, where its variation induced straining on the flame fronts and resulted in the many different topologies across the flames. As for planar flames, since they don't have a mean radius, the effective wrinkling length scale for each flame might be dependant on the flame brush thickness as seen in the conditional averages $\langle\lambda|\mathcal{P}\rangle$ in [9], where the investigated planar flames had different means and deviations in their local λ.

The conditional averages in Fig. 14 show that turbulent motions with local Kolmogorov length, η^* and velocity, $u_\eta{}^*$ scales do not correlate with both $\mathcal{P}$ and $\mathcal{F}$. Consequently, there is no apparent correlation between Kolmogorov scales and both of flame structure and morphology under current turbulent conditions. On the other hand, the gradual decrease in η^* sizes as the turbulence condition shift to the thin reaction zones regime is evident. Although turbulent motions of η^* sizes did not directly contribute to flames' structure and morphology. They may have a contribution to the local flame structure propagation along their vortex tube's axial directions [69]. That can be inferred as ($u_\eta{}^*/u_l$) substantially increased with the increase in Ka.

4 Conclusions

In this study, three-dimensional direct numerical simulations of spherically propagating premixed turbulent stoichiometric hydrogen-air flames were carried out with detailed chemistry and detailed diffusion to clarify the influence of turbulence-flame interactions with respect to flame structure and morphology. This configuration allowed the investigation of developing-flames, which are essential for practical applications. Four cases were computed within the corrugated flamelets and the thin reaction zone regimes. Intense reaction zones of computed cases were quantified, at multiple flame radii, using a mathematical tool based on topological invariants called the shapefinders.

For current stoichiometric hydrogen-air flames, the most significant fuel consumption rate and heat release rate were observed at the highly strained flamelets with negative curvatures. However, the bulk of the fuel was consumed within the positively curved flamelets. Compared to the typically investigated lean hydrogen flame [25, 66], the difference in the location of intense burning was due to the relative richness of the stoichiometric hydrogen flames compared to leaner flames which is reflected in the Lewis number [24]. Despite that H_2 was focused at the positively curved flamelets, the OH radicals were especially focused at the negatively curved flamelets, where they controlled the combustion process through the elementary reaction ($H_2 + OH = H_2O + H$). Therefore, explaining the occurrence of intense reaction zones at the negatively curved flamelets. For all cases $(u_t/u_l) < (A_t/A_l)$, which was due to the reduction in the local burning intensity at the positively curved flamelets as they were subjected to weak tangential strain rates.

The shapefinders showed that intense reaction zones had various shapes, including "tubes", "pancakes" and more complex shapes with larger filamentarity, $\mathcal{F}$. The geometry of intense reaction zones was provided through statistical analysis of the three characteristic scales: thickness, $\mathcal{T}$, width, $\mathcal{W}$, and length, $\mathcal{L}$. As the turbulence level increased, the number of extracted intense reaction zones increased, indicating the increase in the total fuel burning rate, which was due to the broadening of the boundaries of intense reaction zones and forming new ones. As turbulence level increased, thicker, broader, and longer local flame structures were formed at the flame front, and the rates of increasing their surface area (due to straining) was larger compared to their rates of thickening (due to mixing processes). While the mean of the characteristic scales remained unchanged for each flame as it propagated, larger values were obtained at larger flame sizes (especially for $\mathcal{L}$) due to strong small-scale turbulent motions. Furthermore, the difference in geometry/shapes of intense reaction zones between planar and spherical flames was identified in relation to size/volume, local thickness, and local topology, and reasoned based on the differences between the two configurations.

To examine the influence of turbulence-flame interactions at Taylor microscale sizes, the conditional averages of Taylor microscale, conditioned upon the three characteristic scales $\mathcal{T}$, $\mathcal{W}$, and $\mathcal{L}$, as well as the two non-dimensional shapefinders planarity, $\mathcal{P}$ and filamentarity, $\mathcal{F}$ were considered. The conditional averages showed that as turbulent velocity fluctuations and Taylor microscale increased, local flame structures with thinner, broader, and more area coverage were formed at the flame front. Therefore, emphasising on the role of turbulent stretching, especially while considering the increasing gap in value between $\mathcal{W}$ and $\mathcal{L}$ at larger λ^*. Through a comparison, the effect of small-scale turbulence-flame interactions on the surface morphology of developing- and well-developed flames was similar [8, 9]. However, the effect of those interactions concerning the development of the reaction layer and flame thickness was different, as it was prominent, only, in the case of the developing-flame fronts. The results highlighted the importance of turbulent combustion modelling scaled with the small-scale turbulence such as Taylor microscale [72, 76, 77], especially concerning application dealing with developing-flame fronts.

A dissidence was identified between global turbulence statistics and local ones representing the interactions at the flame front. Although turbulence decay held a major role in having lower intensities at the flame front, it would not explain the profile of the local turbulence length scales. Despite the wide range of Taylor microscale across the investigated cases, the variations of local Taylor microscale with the characteristic scales were within the same range, which was reasoned to the flames having the same size. Thus, small-scale local turbulence-flame interactions occurred at a specific Taylor microscales depending on flame size, where effective wrinkling of the flame front occurred, irrelevant of other eddies with larger/smaller length scales, while the variations in wrinkling/straining were controlled by the local velocity fluctuations.

This study was limited to the investigations of flames with small sizes. Therefore, there was no visible change in the value of Taylor microscale at the flame front as the flames propagated. In order to overcome that and to evaluate the evolution of such effective length scale, spherical flames at later stages of flame development should be investigated, which will be the focus of upcoming studies. That being said, the uniqueness of this study remains in confirming a viable methodology to evaluate the temporal evolution of turbulence statistics at the flame front, which proved to be important in describing the local turbulence-flame interactions. Current results can be employed in developing a model that depicts the essential length scales needed to capture local flame shape/topology with specific filter sizes in the combustion model. Furthermore, they can be used to evaluate the combustion's characteristics, including the effect of the sub-grid scale of turbulent flame morphology, by using only the filtered (conditioned) values in the grid scale [9].

Acknowledgements

This work was partially supported by the HPCI System Research Project (Project ID: hp180248). The authors are grateful to Professor Nilanjan Chakraborty of Newcastle University for many inspiring discussions. Y.M. acknowledges the support of JSPS Grant-in-Aid for Young Scientists (B) Grant Number 19K14903.

References

[1] F. C. Gouldin, An Application of Fractais to Modeling Premixed Turbulent Flames, Combustion and Flame 68 (1987) 249–266.

[2] Ö. L. Gülder, G. J. Smallwood, Inner cutoff scale of flame surface wrinkling in turbulent premixed flames, Combustion and Flame 103 (1995) 107–114.

[3] Y. Shim, S. Tanaka, M. Tanahashi, T. Miyauchi, Local structure and fractal character-

istics of H2–air turbulent premixed flame, Proceedings of the Combustion Institute 33 (2011) 1455–1462.

[4] O. Chatakonda, E. R. Hawkes, A. J. Aspden, A. R. Kerstein, H. Kolla, J. H. Chen, On the fractal characteristics of low Damköhler number flames, Combustion and Flame 160 (2013) 2422–2433.

[5] R. Griffiths, J. Chen, H. Kolla, R. Cant, W. Kollmann, Three-dimensional topology of turbulent premixed flame interaction, Proceedings of the Combustion Institute 35 (2015) 1341–1348.

[6] S. Trivedi, R. Griffiths, H. Kolla, J. Chen, R. Cant, Topology of pocket formation in turbulent premixed flames, Proceedings of the Combustion Institute 37 (2019) 2619–2626.

[7] Y. Minamoto, N. Swaminathan, S. R. Cant, T. Leung, Morphological and statistical features of reaction zones in MILD and premixed combustion, Combustion and Flame 161 (2014) 2801–2814.

[8] Y. Minamoto, M. Tanahashi, Effect of turbulent motions at different length scales on turbulent premixed swirl-stabilised flame topology, International Journal of Hydrogen Energy 44 (2019) 22316–22327.

[9] Y. Minamoto, B. Yenerdag, M. Tanahashi, Morphology and structure of hydrogen–air turbulent premixed flames, Combustion and Flame 192 (2018) 369–383.

[10] A. Tyagi, I. Boxx, S. Peluso, J. O'Connor, Statistics and topology of local flame–flame interactions in turbulent flames, Combustion and Flame 203 (2019) 92–104.

[11] M. A. Liberman, M. F. Ivanov, O. E. Peil, D. M. Valiev, L. E. Eriksson, Self-acceleration and fractal structure of outward freely propagating flames, Physics of Fluids 16 (2004) 2476–2482.

[12] K. Mukaiyama, S. Shibayama, K. Kuwana, Fractal structures of hydrodynamically un-

stable and diffusive-thermally unstable flames, Combustion and Flame 160 (2013) 2471–2475.

[13] C. R. Bauwens, J. M. Bergthorson, S. B. Dorofeev, Experimental study of spherical-flame acceleration mechanisms in large-scale propane-air flames, Proceedings of the Combustion Institute 35 (2015) 2059–2066.

[14] A. Lipatnikov, J. Chomiak, Global stretch effects in premixed turbulent combustion, Proceedings of the Combustion Institute 31 (2007) 1361–1368.

[15] M. Weiß, N. Zarzalis, R. Suntz, Experimental study of Markstein number effects on laminar flamelet velocity in turbulent premixed flames, Combustion and Flame 154 (2008) 671–691.

[16] S. Chaudhuri, F. Wu, C. K. Law, Scaling of turbulent flame speed for expanding flames with Markstein diffusion considerations, Physical Review E - Statistical, Nonlinear, and Soft Matter Physics 88 (2013) 1–13.

[17] S. Gashi, J. Hult, K. W. Jenkins, N. Chakraborty, S. Cant, C. F. Kaminski, Curvature and wrinkling of premixed flame kernels-comparisons of OH PLIF and DNS data, Proceedings of the Combustion Institute 30 (2005) 809–817.

[18] D. Thévenin, Three-dimensional direct simulations and structure of expanding turbulent methane flames, Proceedings of the Combustion Institute 30 (2005) 629–637.

[19] K. W. Jenkins, M. Klein, N. Chakraborty, R. S. Cant, Effects of strain rate and curvature on the propagation of a spherical flame kernel in the thin-reaction-zones regime, Combustion and Flame 145 (2006) 415–434.

[20] M. Klein, N. Chakraborty, K. W. Jenkins, R. S. Cant, Effects of initial radius on the propagation of premixed flame kernels in a turbulent environment, Physics of Fluids 18 (2006).

[21] N. Chakraborty, M. Klein, R. S. Cant, Stretch rate effects on displacement speed in

turbulent premixed flame kernels in the thin reaction zones regime, Proceedings of the Combustion Institute 31 (2007) 1385–1392.

[22] M. Klein, N. Chakraborty, R. S. Cant, Effects of turbulence on self-sustained combustion in premixed flame kernels: A direct numerical dimulation (DNS) study, Flow, Turbulence and Combustion 81 (2008) 583–607.

[23] D. T. Dunstan, K. W. Jenkins, Flame surface density distribution in turbulent flame kernels during the early stages of growth, Proceedings of the Combustion Institute 32 (2009) 1427–1434.

[24] G. Ozel-Erol, M. Klein, N. Chakraborty, Lewis Number Effects on Flame Speed Statistics in Spherical Turbulent Premixed Flames, Flow, Turbulence and Combustion 106 (2021) 1043–1063.

[25] A. J. Aspden, M. S. Day, J. B. Bell, Turbulence-chemistry interaction in lean premixed hydrogen combustion, Proceedings of the Combustion Institute 35 (2015) 1321–1329.

[26] A. J. Aspden, A numerical study of diffusive effects in turbulent lean premixed hydrogen flames, Proceedings of the Combustion Institute 36 (2017) 1997–2004.

[27] Ö. L. Gülder, Contribution of small scale turbulence to burning velocity of flamelets in the thin reaction zone regime, Proceedings of the Combustion Institute 31 (2007) 1369–1375.

[28] T. Kulkarni, F. Bisetti, Surface morphology and inner fractal cutoff scale of spherical turbulent premixed flames in decaying isotropic turbulence, Proceedings of the Combustion Institute 38 (2020) 2861–2868.

[29] T. Kulkarni, R. Buttay, M. H. Kasbaoui, A. Attili, F. Bisetti, Reynolds number scaling of burning rates in spherical turbulent premixed flames, Journal of Fluid Mechanics 906 (2021) 1–39.

[30] V. Giovangigli, Convergent iterative methods for multicomponent diffusion, Impact of Computing in Science and Engineering 3 (1991) 244–276.

[31] T. Poinsot, D. Veynante, Theoretical and Numerical Combustion, Second Edition, R.T. Edwards, Philadephia, 2nd edition edition, 2005.

[32] F. A. Williams, Elementary Derivation of the Multicomponent Diffusion Equation, American Journal of Physics 26 (1958) 467–469.

[33] R. Kurose, URL http://www.tse.me.kyoto-u.ac.jp/members/kurose/link_e.php, 2021.

[34] U. Ahmed, C. Turquand D'Auzay, M. Muto, N. Chakraborty, R. Kurose, Statistics of reaction progress variable and mixture fraction gradients of a pulverised coal jet flame using Direct Numerical Simulation data, Proceedings of the Combustion Institute 37 (2019) 2821–2830.

[35] U. Ahmed, A. L. Pillai, N. Chakraborty, R. Kurose, Statistical behavior of turbulent kinetic energy transport in boundary layer flashback of hydrogen-rich premixed combustion, Physical Review Fluids 4 (2019) 103201.

[36] A. L. Pillai, R. Kurose, Combustion noise analysis of a turbulent spray flame using a hybrid DNS/APE-RF approach, Combustion and Flame 200 (2019) 168–191.

[37] A. L. Pillai, J. Nagao, R. Awane, R. Kurose, Influences of liquid fuel atomization and flow rate fluctuations on spray combustion instabilities in a backward-facing step combustor, Combustion and Flame 220 (2020) 337–356.

[38] V. Moureau, C. Bérat, H. Pitsch, An efficient semi-implicit compressible solver for large-eddy simulations, Journal of Computational Physics 226 (2007) 1256–1270.

[39] G. S. Jiang, C. W. Shu, Efficient implementation of weighted ENO schemes, Journal of Computational Physics 126 (1996) 202–228.

[40] P. N. Brown, G. D. Byrne, A. C. Hindmarsh, VODE: A Variable-Coefficient ODE Solver, SIAM Journal on Scientific and Statistical Computing 10 (1989) 1038–1051.

[41] Z. Hong, D. F. Davidson, R. K. Hanson, An improved H2/O2 mechanism based on recent shock tube/laser absorption measurements, Combustion and Flame 158 (2011) 633–644.

[42] T. Passot, A. Pouquet, Numerical simulation of compressible homogeneous flows in the turbulent regime, Journal of Fluid Mechanics 181 (1987) 441.

[43] Z. Chen, Y. Ju, Theoretical analysis of the evolution from ignition kernel to flame ball and planar flame, Combustion Theory and Modelling 11 (2007) 427–253.

[44] J. O. Hinze, Turbulence, McGraw-Hill, 1975.

[45] N. Peters, Turbulent Combustion, Cambridge University Press, Cambridge, 2000.

[46] S. B. Pope, Turbulent Flows, Cambridge University Press, Cambridge, 2000.

[47] P. Clavin, Dynamic behavior of premixed flame fronts in laminar and turbulent flows, Progress in Energy and Combustion Science 11 (1985) 1–59.

[48] C. Law, C. Sung, Structure, aerodynamics, and geometry of premixed flamelets, Progress in Energy and Combustion Science 26 (2000) 459–505.

[49] D. Bradley, R. a. Hicks, M. Lawes, C. G. W. Sheppard, R. Woolley, The measurement of laminar burning velocities and Markstein numbers for iso-octane-air and iso-octane-n-heptane-air mixtures at elevated temperatures and pressures in an explosion bomb, Combustion and Flame 115 (1998) 126–144.

[50] T. Kitagawa, T. Nakahara, K. Maruyama, K. Kado, A. Hayakawa, S. Kobayashi, Turbulent burning velocity of hydrogen–air premixed propagating flames at elevated pressures, International Journal of Hydrogen Energy 33 (2008) 5842–5849.

[51] M. Matalon, Flame dynamics, Proceedings of the Combustion Institute 32 (2009) 57–82.

[52] P. Brequigny, C. Endouard, C. Mounaïm-Rousselle, F. Foucher, An experimental study on turbulent premixed expanding flames using simultaneously Schlieren and tomography techniques, Experimental Thermal and Fluid Science 95 (2018) 11–17.

[53] S. Osher, F. Ronald, Level Set Methods and Dynamic Implicit Surfaces, Springer, New York, 2003.

[54] D. Veynante, L. Vervisch, Turbulent combustion modeling, Progress in Energy and Combustion Science 28 (2002) 193–266.

[55] H. Minkowski, Volumen und Oberflache, Mathematische Annalen 57 (1903) 447–495.

[56] T. Leung, N. Swaminathan, P. A. Davidson, Geometry and interaction of structures in homogeneous isotropic turbulence, Journal of Fluid Mechanics 710 (2012) 453–481.

[57] J. Schmalzing, T. Buchert, Beyond Genus Statistics: A Unifying Approach to the Morphology of Cosmic Structure, The Astrophysical Journal 482 (1997) L1–L4.

[58] V. Sahni, B. S. Sathyaprakash, S. F. Shandarin, Shapefinders: A New Diagnostic For Large-scale Structure, The Astrophysical Journal 495 (1998) 5–8.

[59] H. Trac, D. Mitsouras, P. Hickson, R. Brandenberger, Topology of the Las Campanas Redshift Survey, Monthly Notices of the Royal Astronomical Society 330 (2002) 531–539.

[60] J. V. Sheth, V. Sahni, S. F. Shandarin, B. S. Sathyaprakash, Measuring the geometry and topology of large-scale structure using SURFGEN: Methodology and preliminary results, Monthly Notices of the Royal Astronomical Society 343 (2003) 22–46.

[61] N. Chakraborty, S. Cant, Unsteady effects of strain rate and curvature on turbulent premixed flames in an inflow-outflow configuration, Combustion and Flame 137 (2004) 129–147.

[62] C. J. Rutland, A. Trouvé, Direct simulations of premixed turbulent flames with nonunity Lewis numbers, Combustion and Flame 94 (1993) 41–57.

[63] T. Echekki, J. H. Chen, Unsteady strain rate and curvature effects in turbulent premixed methane-air flames, Combustion and Flame 106 (1996) 184–190.

[64] N. Peters, P. Terhoeven, J. H. Chen, T. Echekki, Statistics of flame displacement speeds from computations of 2-D unsteady methane-air flames, Symposium (International) on Combustion 27 (1998) 833–839.

[65] Chun k. Law, Combustion Physics, Cambridge University Press, Cambridge, 2006.

[66] A. J. Aspden, M. S. Day, J. B. Bell, Turbulence-flame interactions in lean premixed hydrogen: Transition to the distributed burning regime, Journal of Fluid Mechanics 680 (2011) 287–320.

[67] P. D. Ronney, V. Yakhot, Flame broadening effects on premixed turbulent flame speed, Combustion Science and Technology 86 (1992) 31–43.

[68] V. L. Zimont, Theory of turbulent combustion of a homogeneous fuel mixture at high reynolds numbers, Combustion, Explosion, and Shock Waves 15 (1979) 305–311.

[69] A. N. Lipatnikov, J. Chomiak, Molecular transport effects on turbulent flame propagation and structure, Progress in Energy and Combustion Science 31 (2005) 1–73.

[70] S. Yang, A. Saha, W. Liang, F. Wu, C. K. Law, Extreme role of preferential diffusion in turbulent flame propagation, Combustion and Flame 188 (2018) 498–504.

[71] B. Renou, A. Boukhalfa, D. Puechberty, M. Trinité, Local scalar flame properties of freely propagating premixed turbulent flames at various Lewis numbers, Combustion and Flame 123 (2000) 507–521.

[72] R. G. Abdel-Gayed, K. J. Al-Kishali, D. Bradley, Turbulent Burning Velocities and Flame Straining in Explosions., Proceedings of The Royal Society of London, Series A: Mathematical and Physical Sciences 391 (1984) 393–414.

[73] N. Chakraborty, R. S. Cant, Effects of Lewis number on turbulent scalar transport and its modelling in turbulent premixed flames, Combustion and Flame 156 (2009) 1427–1444.

[74] R. Yu, T. Nillson, X. S. Bai, A. N. Lipatnikov, Evolution of averaged local premixed flame thickness in a turbulent flow, Combustion and Flame 207 (2019) 232–249.

[75] A. Lipatnikov, J. Chomiak, Turbulent burning velocity and speed of developing, curved, and strained flames, Proceedings of the Combustion Institute 29 (2002) 2113–2121.

[76] B. Lewis, G. von Elbe, Combustion, Flames and Explosions of Gases, Academic Press, New York and London, 2nd editio edition, 1961.

[77] R. A. Strehlow, Combustion Fundamentals, McGraw-Hill, New York, 1984.